Complex-ordered patterns in shaken convection

Jeffrey L. Rogers,[1,2] Werner Pesch,[3] Oliver Brausch,[3] and Michael F. Schatz[2]

[1]*HRL Laboratories, LLC, Malibu, California 90265, USA*

[2]*Center for Nonlinear Science and School of Physics, Georgia Institute of Technology, Atlanta, Georgia 30332-0430, USA*

[3]*Physikalisches Institut der Universität Bayreuth, Bayreuth, Germany 95440*

We report and analyze complex patterns observed in a combination of two standard pattern forming experiments. These exotic states are composed of two distinct spatial scales, each displaying a different temporal dependence. The system is a fluid layer experiencing forcing from both a vertical temperature difference and vertical time-periodic oscillations. Depending on the parameters these forcing mechanisms produce fluid motion with either a harmonic or a subharmonic temporal response. Over a parameter range where these mechanisms have comparable influence the spatial scales associated with both responses are found to coexist, resulting in complex, yet highly ordered patterns. Phase diagrams of this region are reported and criteria to define the patterns as quasiperiodic crystals or superlattices are presented. These complex patterns are found to satisfy four-mode (*resonant tetrad*) conditions. The qualitative difference between the present formation mechanism and the resonant triads ubiquitously used to explain complex-ordered patterns in other nonequilibrium systems is discussed. The only exception to quantitative agreement between our analysis based on Boussinesq equations and laboratory investigations is found to be the result of breaking spatial symmetry in a small parameter region near onset.

I. INTRODUCTION

Convective systems have played an essential role in developing understanding of nonlinear dynamics and spatially extended systems. To study system states that form as well as transitions between them one typically begins with a uniform state and increases the stress on the system. As this stress increases past some critical value, spatial or temporal variations form that are commonly described as patterns [1]. These studies often focus on the initial (primary) regular variations that possess a single characteristic wave number. Onset values of both the stress parameter and critical wave number (q_c) are found by linear stability analysis of the uniform state. The planforms of stable patterns are then dictated by nonlinear mode interactions. Observed planforms are usually basic near primary onset, stripes, squares, or hexagons [2,3] and do not include more than two basic wave vectors. Further increasing system stress produces more complex patterns [4]. Secondary bifurcations that break spatial or temporal symmetries are often responsible for this additional complexity. Symmetry breaking can produce multimode patterns, aperiodic states, and turbulence [5,6]. However, even if the original stationary patterns remain stable, the presence of competing attractors may lead to persistent dynamics as a result of long wavelength distortions, emergence of multiple domains, dislocations, as well as other pattern defects. Modern examples include spiral-defect chaos [2] and defect turbulence [7].

Recently, pattern formation studies have extended the single wave-number focus to include what Pismen [8] has termed complex-ordered states. While these patterns are spatially complicated, in the spectral domain they are described by a relatively small number of Fourier modes. If the spectral peaks are incommensurate in wave number the state is a quasiperiodic crystal pattern [9] (see Sec. VI). In the special case where the peaks are commensurate the resulting periodic pattern is a superlattice. Typically these states are composed of a regular arrangement of short scale subunits on a larger scale backbone. Quasiperiodic crystals, sometimes referred to as quasipatterns, and superlattices have been reported in various hydrodynamic [10–15] and optical systems [16,17]. In the hydrodynamic cases the distinct wave numbers of relevant spectral modes naturally arise in the vicinity of a bicritical point where distinct bifurcation routes of the unstructured ground state coexist. Additionally, (near)-resonant interactions of the basic pattern forming modes with certain weakly damped modes of different wave number may come into play [18]. The optical cases are conceptually different. In these cases light waves of different wavelengths are selectively generated and superimposed by a feedback mechanism.

The focus of this paper is a separate pattern forming system that also possesses a bicritical point; thermal convection in the presence of vertical oscillations. In particular, we are interested in a fluid layer of depth d and relatively large lateral extent, driven by both an imposed vertical temperature difference and vertical oscillations (Fig. 1). If only the thermal driving is present the system reduces to a standard Rayleigh-Bénard experiment, which is commonly used in convection and pattern formation studies [1,2]. In this case fluid motion begins at a well-defined temperature difference ($\Delta T = \Delta T_c$) and becomes more complex with increasing ΔT. Only two nondimensional parameters are required for the theoretical description, the Rayleigh number $R = \alpha g d^3 \Delta T / \nu \kappa$ and the Prandtl number $\mathrm{Pr} = \nu / \kappa$. In the definitions of Pr and R are the kinematic viscosity ν, thermal diffusivity κ, thermal expansivity α, and the earth's gravitational acceleration g. The characteristic length scale is set by
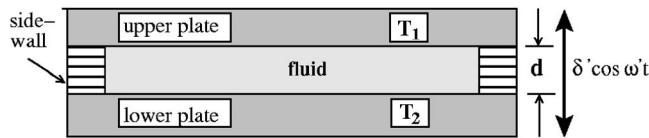
FIG. 1. Fluid motion in the layer is driven both by the imposed temperature difference $\Delta T = T_2 - T_1$ and vertical oscillations of the form $\delta' \cos \omega' t$. In addition to the standard Rayleigh-Bénard parameters of Pr and R this system is characterized by two nondimensional modulation parameters $\delta \mathrm{Fr}$ and ω (see text).

d, with the characteristic time scale being the vertical diffusion time $t_v = d^2/\kappa$. Due to the working fluid in this study being a compressed gas $\mathrm{Pr} \approx 1$. Precisely $\mathrm{Pr} = 0.930$, unless otherwise stated.

If only the vertical oscillations are imposed the system does not display patterns. Unlike a Faraday experiment that studies surface wave formation [10–15], the present system does not have a free surface. Thereby, in the absence of the thermal driving the uniform state is stable. Inclusion of the parametric forcing produces an effective modulated gravity and requires two additional dimensionless (modulation) parameters, angular frequency $\omega = t_v \omega'$ and displacement amplitude $\delta \mathrm{Fr} = \delta'/gt_v^2 = (\kappa^2/d^4 g)\delta'$. In the laboratory the displacement amplitude δ' and the angular frequency ω' are measured.

Linear stability analyses [19–23] of the Boussinesq equations for shaken convection indicate that flows with two distinct temporal and spatial scales can be stimulated. Our description of vertically oscillated convection is based on standard Boussinesq equations with an appropriate modulated gravity term and produces excellent agreement with the experiments. In both cases of (i) heating from below [$R > 0$, Figs. 2(a) and 2(b)] and (ii) heating from above [$R < 0$, Figs. 2(c) and 2(d)], these studies predict primary onset occurs to fluid flows possessing time dependence proportional to the modulation frequency. Onset to flows synchronous to the drive period ($\tau = 2\pi/\omega$) or *harmonic* occurs at relatively smaller values of the modulation parameters, while at larger values of $\delta \mathrm{Fr}$ and ω primary onset occurs to flows periodic at 2τ or *subharmonic*. In case (i) harmonic flows are more stable than in the absence of modulation, i.e., the critical Rayleigh number for harmonic primary onset R_c^H is expected to be larger than the critical Rayleigh number in the absence of modulation ($R_c^0 = 1708$). Subharmonic flows may occur at a Rayleigh number either larger ($R_c^S > R_c^0$) or smaller ($R_c^S < R_c^0$) than unmodulated convection. In this case the wave number at harmonic onset is less than at subharmonic onset ($q_c^H < q_c^S$). In case (ii) primary onset again may occur to either harmonic or subharmonic flows. In contrast to case (i), subharmonic wave numbers at onset are smaller than the harmonic ones ($q_c^S < q_c^H$). In the $\delta \mathrm{Fr}$-R parameter space harmonic and subharmonic threshold curves cross at a bicritical point ($\delta \mathrm{Fr} = \delta_{2c} \mathrm{Fr}$, $R = R_{2c}$).

Describing the current system by analogy to a pendulum with an oscillating base provides a qualitative understanding of the onset behavior. Mathematically this description is in terms of a Mathieu equation [19]. Case (i) corresponds to an inverted pendulum while case (ii) can be mapped onto the
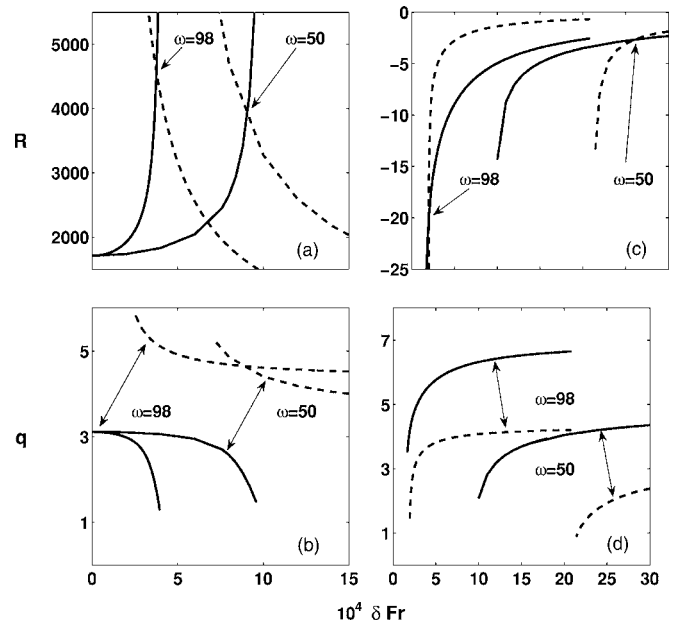

FIG. 2. Results from our linear stability analysis of vertically oscillated Rayleigh-Bénard convection for the cases of heating from below [(a) and (b)] and from above [(c) and (d)]. Solid lines are the harmonic marginal stability boundaries (R_c^H, q_c^H), while dashed curves are the corresponding subharmonic boundaries (R_c^S, q_c^S) for two frequencies, $\omega = 98$ and 50. Arrows in (a) and (c) point to the bicritical points where harmonic and subharmonic threshold curves intersect at $\delta_{2c} \mathrm{Fr}$, R_{2c}. Corresponding critical wave numbers are shown in (b) and (d).

hanging pendulum. Stabilization of an inverted pendulum by oscillating its base is an example of modulation induced stability. In case (ii), $\Delta T = T_2 - T_1 < 0$, the resulting Rayleigh number R is negative and no convection occurs in the absence of modulation. However, for sufficiently large $|\Delta T|$ damped *internal waves* exist, which are relatively long lived, due to the decay time being considerably larger than the temporal period. In fact, due to a resonant coupling of these modes to the externally modulated gravity, a convection instability can be excited as well. The primary onset properties of this case, which we will briefly address in the paper, are shown in Figs. 2(c) and 2(d).

Symmetry properties play an important role in the selection of the stable pattern near onset. The properties of the emerging state are captured by a Landau-type equation for the pattern amplitude A. In the Boussinesq approximation of Rayleigh-Bénard convection, temperature variations of the material parameters, with the exception of the buoyancy term, are neglected. Thereby, the system is invariant against spatial reflections about the fluid layer midplane. This spatial symmetry requires the amplitude equations be invariant under the transformation $A \rightarrow -A$. As a result even order terms are excluded from the equations. Corresponding stripes are usually observed at threshold, although in a few examples squares have been observed [24–27]. If Boussinesq symmetry is violated, quadratic terms allow two modes to resonate with a third, forming a *resonant triad*, and hexagons will form close to threshold [3]. In contrast to the described spatial symmetry, parametrically driven systems typically pos-

sess a symmetry under discrete time translation by a drive period τ. If the response of the system is subharmonic, the amplitude equations must be invariant under the transformation $A \to -A$, which again precludes quadratic terms and three-mode interactions. On the other hand, in the case of harmonic response or if the time translation invariance is broken resonant triads are again allowed and can generate a whole variety of complex-ordered patterns, provided they are not excluded by spatial symmetries.

In contrast to the majority of complex-ordered patterns observed previously in parametrically driven systems we find quasiperiodic crystalline and superlattice states near primary onset in the presence of inversion symmetry [23]. A commonly observed pattern in the current system is a quasiperiodic crystal composed of starlike structures on a square background. These complex-ordered states are found over a relatively wide parameter range in both experiments and simulations that are in quantitative agreement over the majority of the studied parameter space. The one exception occurs in the vicinity of bicriticality where numerics with Boussinesq symmetry indicate such complex-ordered patterns may emerge directly from conduction at the bicritical point. However, these are not observed in the laboratory. The discrepancy is found to be due to non-Boussinesq effects in the experiments close to bicriticality.

This paper is divided into sections based on topic. In Sec. II A our experimental apparatus is presented, while our numerical methods are described in Sec. II B. The transitions to complex-ordered patterns from conduction (Sec. III A) as well as from states of either pure harmonic (Sec. III B) or pure subharmonic convection (Sec. III C) for a representative ω are then presented. In Sec. IV four-mode resonance mechanisms (*resonant tetrads*) that produce the observed patterns are presented and discussed. In Sec. V A complex-ordered patterns found in both experiments and simulations at other ω values are examined. All of our experiments and the majority of numerics consider the case of heating from below ($R > 0$). These results are augmented in Sec. V B with analysis findings for heating from above. The mathematical characterization of the complex-ordered patterns we observed is presented in Sec. VI. Finally, conclusions and complementary discussions are presented in Sec. VII.

II. BACKGROUND

A. Experimental apparatus

Our convection apparatus is based on well-tested designs for standard Rayleigh-Bénard convection using compressed gases [28,29]. The convection cell (Fig. 3) is inside a hollow cylinder with a mirror for the bottom surface and a sapphire crystal for the upper surface. The mirror is a gold coated cylindrical aluminum block 5.08 cm in diameter and 0.60 cm thick. The sapphire crystal is also cylindrical with a 5.0 cm diameter and height of 2.54 cm. Between the surfaces the lateral boundary (side wall) of the convection cell is a vertical stack of filter paper with an inner diameter of 3.8 cm and an outer diameter of 5.08 cm; the thickness of the filter paper stack determines the gas layer thickness d which is typically
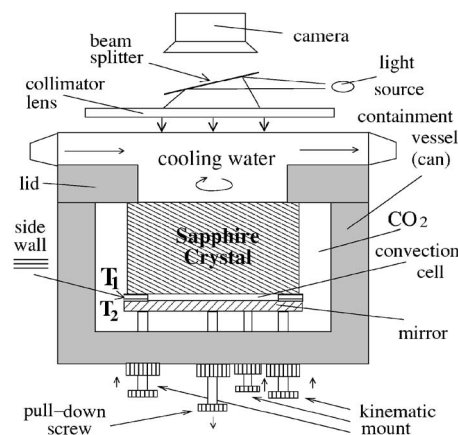

FIG. 3. Sketch of the experimental apparatus (not to scale) including the imaging method, location of cooling water, pressurized containment can, and kinematic mount.

in the range of 0.05 to 0.07 cm. The corresponding vertical diffusion time is $t_v = d^2/\kappa \approx 1.5$ s.

The convection cell is confined in an aluminum pressure containment vessel that is 6.75 cm high with a 6.93 cm inner diameter and an 8.95 cm outer diameter. The sapphire crystal is held tightly against the top of the vessel by the pressure of the compressed CO_2 gas contained inside. The aluminum mirror is aligned parallel to the bottom of the sapphire crystal by a kinematic mount consisting of three fine-adjustment screws arranged in a centered equilateral triangle. A fourth adjustment screw is attached to the center of the mirror bottom, allowing the aluminum mirror to be tightened against the kinematic mount to ensure that the mirror does not move once the cell surfaces have been adjusted parallel to one another. Cell surfaces are aligned by interferometry using a He-Ne laser as a light source (Fig. 3). A set of fringes is produced by the light reflected from the lower sapphire crystal surface and the upper (reflective) surface of the mirror allowing leveling to within a few optical wavelengths. Interferometry measurements demonstrate that the bounding surfaces remain level when oscillations are imposed. Systematically exploring the parameter space of Pr, R, ω, and δFr requires control over temperatures and pressure in the convection cell as well as the vertical oscillations of the apparatus.

We control around two temperatures in the convection cell. Both the vertical temperature difference (ΔT) and the mean temperature ($\bar{T}$) are controlled by linear proportional-integral-derivative schemes that vary the heating of the bottom mirror and the cooling of the sapphire crystal. Heat is supplied by a resistive heater attached to the mirror bottom, while a temperature-controlled water bath circulates water through a closed chamber attached to the top of the containment vessel to cool the sapphire crystal. Uniform cooling is verified by measuring the water temperatures at numerous locations in the water chamber while constant power is supplied to the mirror heater. Typically, $\bar{T}$ is held fixed while ΔT is either varied or also held fixed. Using this approach both $\bar{T}$ and ΔT are maintained to within $\pm 0.01\,^\circ$C. Varying ΔT provides proportional changes in the parameter R, while main-

taining a constant $\bar{T}$ fixes the material parameters, facilitating systemic investigation of the nondimensional parameter space.

Typically convection cell pressure is maintained at 32.72 bars by supplying compressed gas from a reservoir in a upstream cylinder filled with 99.99% pure CO_2. The pressure in the cell is controlled by varying the heat to a small gas reservoir downstream from the convection apparatus. The pressure in the convection apparatus is regulated with an accuracy better than ±0.01 bars under computer control using a high-resolution pressure sensor (SensoTec TJE/3883-12TJA) while varying the reservoir temperature (and, hence, the pressure) with a heating pad.

Vertical oscillations of the convection cell are generated by custom designed hydraulic-shaker systems manufactured by Team Corporation, Burlington, WA. The convection apparatus is attached to a piston whose motion is driven by the flow of oil at high pressure (120 bars). Oil flow is regulated by high performance electrodynamic servo valves which are driven by an amplifier under closed loop control. Thus, controlled oscillations of the piston are achieved by feeding an oscillatory control voltage signal into the amplifier. The displacement amplitudes of the oscillations are measured by a linear variable displacement transducer (LVDT) attached directly to the piston. These measurements are augmented by an accelerometer attached to the base of the convection apparatus which records instantaneous accelerations. The hydraulic shaker is rigidly attached to a heavy mount (ballast), which in turn, rests on elastic supports to damp out vibrational recoil.

Two different shaker assemblies are utilized. The bulk of the experiments are performed using a hydraulic shaker with maximum vertical stroke of ≈ 4 cm that is directly coupled to the convection apparatus using a rigid mounting bracket. In this arrangement, the convection apparatus exhibits horizontal motions that are typically 0.04–0.08 cm; moreover, the piston and apparatus are able to rotate slightly in a horizontal plane. A limited number of studies are performed using a second hydraulic shaker with a maximum stroke of ≈ 15 cm that is connected to the apparatus using a rectangular air bearing assembly. This configuration prevents rotation and reduces lateral vibrations to approximately 0.008 cm.

Patterns are visualized using the established method of shadowgraphy [28,29]. Compressed gases greatly enhance the sensitivity of the shadowgraph [28] by refractive index reinforcement and the relatively thin layers that may be studied. Shadowgraph images are captured using a CCD camera interfaced with a computer controlled frame grabber. The image acquisition is synchronized with the shaker drive by use of a ferroelectric liquid crystal shutter. Pattern images are acquired at a predefined phase of the oscillation that may be varied.

Recorded images are analyzed predominately in terms of spectral quantities. The time series of images recorded at each fixed set of parameters are analyzed for the average spectral components. Initially a background mask and a radial Hanning function are applied to each image to reduce aliasing. After recording the variance of the processed image a spatial Fourier transform is performed and the constituent

phase angles and power spectrum are found. Generally, the power spectrum is normalized by the processed image variance so that the total power in the spectrum will sum to unity. The power spectrum is then azimuthally averaged to produce the radial spectrum $[\wp(q)]$. Radial power spectra for all the images at a data point are then averaged to produce $\langle \wp(q) \rangle$ and subsequently used to calculate the first two moments of the resulting distribution function in q,

$$\langle q \rangle = \frac{\int_0^\infty q^2 \langle \wp(q) \rangle dq}{\int_0^\infty q \langle \wp(q) \rangle dq}, \tag{1}$$

$$\langle q^2 \rangle = \frac{\int_0^\infty q^3 \langle \wp(q) \rangle dq}{\int_0^\infty q \langle \wp(q) \rangle dq}. \tag{2}$$

The global properties of the patterns at a given set of parameters may then be condensed into three spectral quantities, the relative power, characteristic wave number ($q = \langle q \rangle$), and the width of the wave number distribution ($\sigma = \sqrt{\langle q^2 \rangle - \langle q \rangle^2}$). In patterns with several prominent wave numbers, eighth-order Butterworth filters are applied to remove frequency components outside those being considered.

B. Numerical methods

The convective flow is governed by the Oberbeck-Boussinesq equations. In the frame comoving with the oscillated layer the nondimensional form of these equations is

$$\nabla \cdot \mathbf{v} = 0,$$

$$\nabla^2 \mathbf{v} + \hat{\mathbf{z}}\left(1 + \frac{\delta' \omega'^2}{g} \cos \omega t\right)\Theta - \nabla P = \frac{1}{\text{Pr}}\left(\mathbf{v} \cdot \nabla \mathbf{v} + \frac{\partial \mathbf{v}}{\partial t}\right),$$

$$\nabla^2 \Theta + R\hat{\mathbf{z}} \cdot \mathbf{v} = \mathbf{v} \cdot \nabla \Theta + \frac{\partial \Theta}{\partial t}, \tag{3}$$

written in terms of the velocity $\mathbf{v}$, the temperature deviation Θ from the applied temperature profile, and the pressure P. To nondimensionalize the equations the spatial scale d and temporal scale t_v are used. The effect of modulation appears only in the additional time dependent buoyancy term $\hat{\mathbf{z}}(\omega^2 \delta \text{Fr} \cos \omega t)\Theta$ [19,20]. The so-called up-down Boussinesq symmetry is not broken by the modulation. The equations are solved using realistic isothermal ($\Theta = 0$) and no slip ($\mathbf{v} = \mathbf{0}$) boundary conditions at the confining upper and lower plates. The incompressibility condition $\nabla \cdot \mathbf{v} = 0$ is satisfied by the introduction of a poloidal and a toroidal velocity potential.

For the characterization of two-dimensional roll solutions, we follow the standard Galerkin approach [20]. The boundary conditions at the plates are enforced by expanding all fields with respect to the vertical coordinate z in appropriate

test functions (trigonometric or Chandrasekhar functions). The dependence on the horizontal coordinates (periodic boundary conditions) and on the time t are captured by Fourier expansions. Linearization permits calculation of the critical Rayleigh number and the critical wave number as function of δFr and ω (Fig. 2). The weakly nonlinear regime is investigated on the basis of amplitude equations. In select cases we confirm the numerical simulations by constructing nonlinear roll solutions and examining these for secondary bifurcations. Our computations are found to be in quantitative agreement with previously published results [20,21,30] for all the test cases that we examined.

To interpret the present experiments we found it was necessary to perform direct three-dimensional numerical simulations of Eqs. (3). In contrast to the prior numerical investigation [31] that focused only on a small box with two rolls, we find that assessing the resonant tetrad mechanism to be discussed in the text requires a relatively large horizontal extension. Only minor modifications are required to explicitly integrate in time the time-dependent buoyancy (a linear term) together with the quadratic nonlinearities [30]. All the simulations reported are based on our well-tested code for standard Rayleigh-Bénard convection [2,30]. Typically, only periodic boundary conditions are used in the lateral directions. In some cases we include non-Boussinesq effects using the same approach employed for standard Rayleigh-Bénard convection [2,3]. The essence of the approach is to expand the temperature dependence of all material parameters about $\bar{T}$ to linear order. This results in non-Boussinesq correction terms familiar from standard Rayleigh-Bénard convection [2] and in a modification of the time-dependent buoyancy term via the temperature dependence (at quadratic order) of the density. In these cases an additional circular ramp in applied temperature gradient is introduced to the periodic lateral boundary condition [2] to match the experimental convection cells.

Previously reported results for vertically oscillated convection with heating from above have been limited to numerical investigations of convection onset and the stability of rolls [19,31]. Complex patterns have only been addressed by Volmar and Müller [32], who utilized a weakly nonlinear amplitude equation model with *ad-hoc* quadratic non-Boussinesq terms to predict the existence of some hexagonal-type quasiperiodic crystals. In contrast, our simulations establish the existence of complex convection patterns on the basis of Boussinesq equations.

III. TRANSITION TO SQUARE QUASIPERIODIC CRYSTALS

Within the parameter space region bounded by the harmonic and subharmonic marginal stability curves for R larger than R_{2c}, where these curves intersect [Fig. 2(a)], modes of the two temporal responses coexist. Interactions between the coexisting harmonic and subharmonic patterns produce complex-ordered states. Examples observed at $\omega \approx 100$ are shown in Figs. 4(a) and 4(b). We call a pattern of this type a *square quasiperiodic crystal* (SQC). Like most of the complex-ordered patterns found in this investigation SQCs
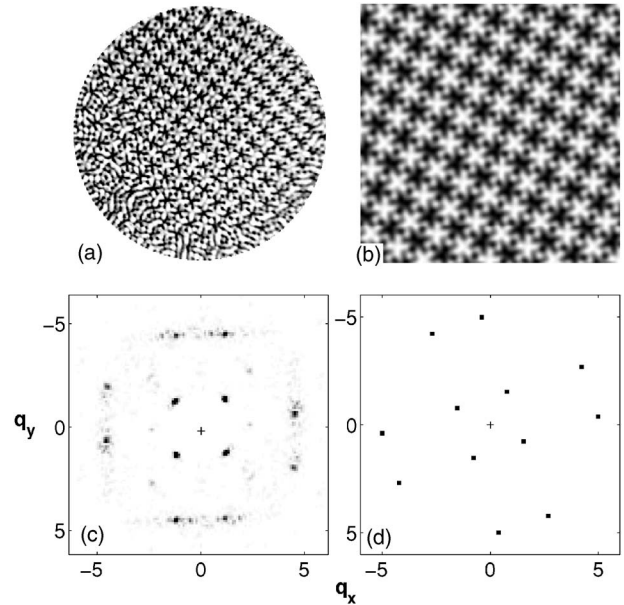

FIG. 4. A square quasiperiodic crystal and a square superlattice observed in (a) experiment and (b) Boussinesq simulation, respectively. Parameter values are (a) δFr$=3.88 \times 10^{-4}$, $\omega=95.3$, $R=7030$ and (b) δFr$=3.75 \times 10^{-4}$, $\omega=98$, $R=4750$. Power spectra for the experimental (c) and numerical (d) patterns both display 12 prominent peaks in Fourier space, $\mathbf{q}=(q_x, q_y)$.

are generally quasiperiodic structures [Fig. 4(a)] that become strictly periodic when constraints, to be introduced in Sec. VI, on the dominant wave vectors are satisfied. We refer to the periodic form of an SQC states as a *square superlattice* (SQL); an example of an SQL is shown in Fig. 4(b). In the experiments, nearly defect free SQCs, like that shown in Fig. 4(a), form between $R=6280$ up to the maximum experimentally accessible $R \approx 9300$. Simulations find SQCs over a widening range of δFr for R increasing from the bicritical point. Results from experimental and numerical mappings of the parameter range of stable SQCs are summarized in Fig. 5.

In the following, we report experiments and simulations designed to investigate the formation of SQCs. To this end results are presented near a specific shaking frequency ($\omega \approx 100$) where the bicritical point occurs at $R_{2c} \approx 4500$, δ_{2c}Fr$\approx 3.8 \times 10^{-4}$ and the critical wave numbers are $q_c^H \approx 1.8$ and $q_c^S \approx 5.15$. Section III A examines the transition from the conduction state to complex-ordered convection. We find evidence of primary onset to complex order at bicritical points. In these investigations Pr, ω, and δFr $\approx \delta_{2c}$Fr are held relatively constant while R is varied. Section III B describes the transition from purely harmonic convection to complex order observed when increasing δFr at fixed Pr, ω, and R. Finally, by decreasing δFr at fixed Pr, ω, and R we report on the transition from pure subharmonic patterns to complex order in Sec. III C. Along these routes one observes various disordered mixed states composed of harmonic and subharmonic modes, as well as sharp transitions to SQCs. We find that the disorder-order transitions are clearly reflected in abrupt changes of the power spectra.
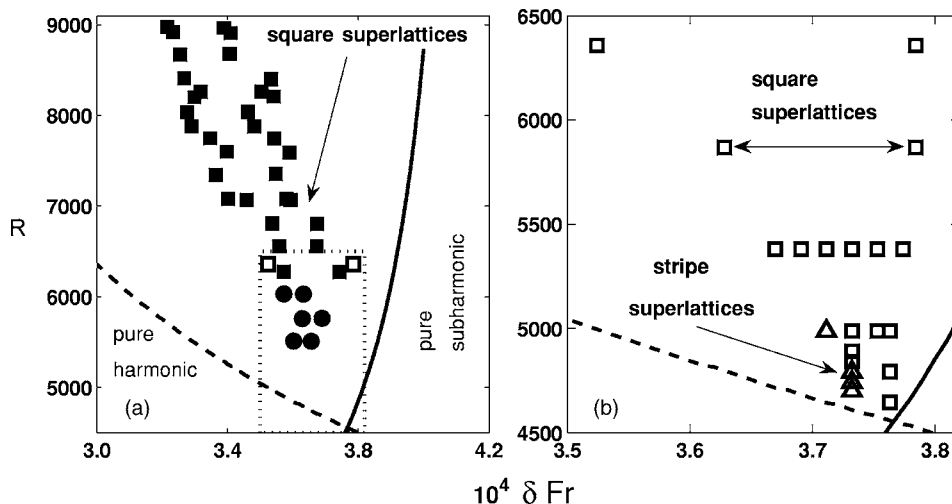
FIG. 5. Phase plane boundaries for complex-ordered patterns observed in (a) experiments and (b) Boussinesq numerics at $\omega = 98.0$. In experiments SQCs are observed over the parameter range bounded by ■ with $R \gtrsim 6300$. At lower R values experiments find spatially complex patterns (●) composed of patches with several cellular symmetries in the harmonic component. Boundaries found in Boussinesq numerics are denoted by □ for SQCs and △ for stripe superlattices (these are discussed in Sec. III A). The dotted box in (a) is the parameter range shown in (b). SQC boundary lines from experiments compare well with boundaries found in Boussinesq numerics for $R \gtrsim 6280$; for example, the numerical (□) and experimental (■) boundaries are compared at $R \approx 6300$ in (a).

A. Transition from conduction

Both experiments and simulations maintaining Boussinesq symmetry find parallel stripes at primary onset for both purely harmonic ($\delta \mathrm{Fr} < \delta_{2c}\mathrm{Fr}$) and purely subharmonic ($\delta \mathrm{Fr} > \delta_{2c}\mathrm{Fr}$) flows. Simulations find SQCs very near the bicritical point at $\omega = 98$ ($\delta_{2c}\mathrm{Fr} = 3.77 \times 10^{-4}$ and $R_{2c} = 4565$). In particular at $\delta \mathrm{Fr} = \delta_{2c}\mathrm{Fr}$ these complex-ordered states are found to bifurcate directly from the conduction state at $R = R_{2c}$. Both harmonic and subharmonic modes contain virtually equal spectral power, which increases continuously from zero as $\sqrt{R - R_{2c}}$, i.e., the complex-ordered patterns bifurcate supercritically from conduction. As R increases, the range of $\delta \mathrm{Fr}$ where SQCs are attracting becomes wider [Fig. 5(b)]. A second type of complex-ordered pattern [Fig. 6(a)], namely *stripe superlattices*, arises for increasing R near the bicritical point when $\delta \mathrm{Fr} < \delta_{2c}\mathrm{Fr}$. They bifurcate supercritically from the base state of harmonic stripes and are found to contain six spectral modes, a harmonic pair and two subharmonic pairs [Fig. 6(b)]. Stripe superlattices are found to be bistable with SQCs over a relatively narrow parameter range [Fig. 5(b)].

When the temperature dependence of fluid properties (i.e., ν, κ, etc.) within the fluid layer cannot be neglected in nonoscillating Rayleigh-Bénard convection the transition to stripes is, in principle, preempted by a subcritical transition to hexagons due to the non-Boussinesq effects. However, in experiments at moderate ΔT_c the hexagon state is often not resolved, since it becomes unstable to rolls (stripes) very near to onset, which are typically observed [2]. Hexagon patterns are also expected in the oscillating case near onset. In fact they have been clearly seen in experiments [Fig. 7(a)] near the bicritical point in the harmonic regime where ΔT_c (≈ 17 °C) and thus the non-Boussinesq effects are expected to be significant. As mentioned in the Introduction, subharmonic hexagons are excluded by temporal symmetry. The harmonic hexagons in the oscillating case have been confirmed in numerical simulations for $\delta \mathrm{Fr} \lesssim \delta_{2c}\mathrm{Fr}$ as well. An example relatively close to the codimension-2 point is shown in Fig. 7(b).
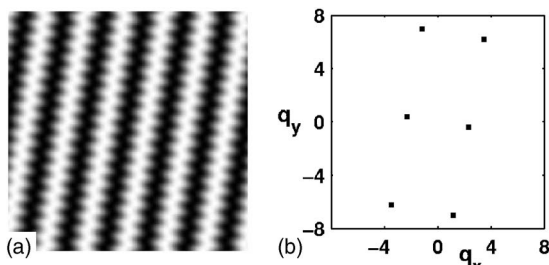

FIG. 6. Boussinesq simulations find a periodic complex-ordered pattern over a narrow parameter range [Fig. 5(b)]. These (a) stripe superlattices ($\delta \mathrm{Fr} = 3.732 \times 10^{-4}$, $\omega = 98$, $R = 4794$) are constructed of (b) six modes.
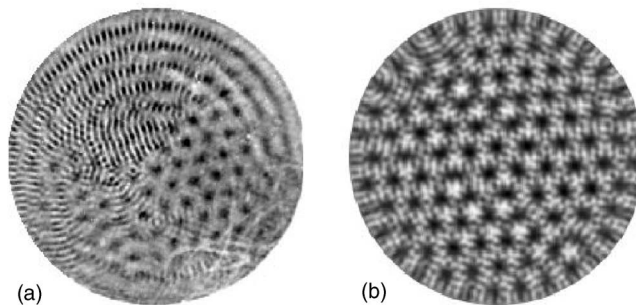

FIG. 7. Coexistence patterns close to bicriticality display hexagons in the harmonic component when non-Boussinesq effects are present. Similar observations are made in both (a) experiments ($\delta \mathrm{Fr} = 3.77 \times 10^{-4}$, $\omega = 97.3$, $R = 4946$) and (b) non-Boussinesq simulations that include an additional circular ramp in the periodic boundary conditions ($\delta \mathrm{Fr} = 3.75 \times 10^{-4}$, $\omega = 98$, $R = 4750$).
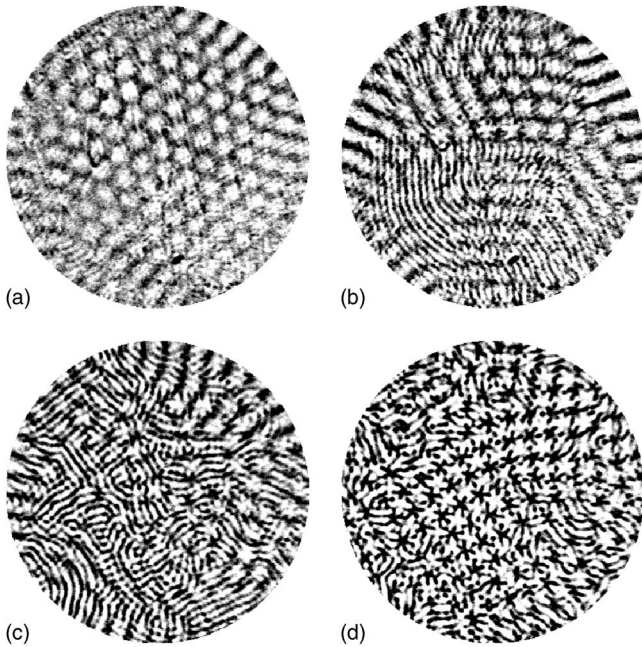
FIG. 8. Patterns (*experiment*) observed passing from conduction to convection by slowly increasing R at $\delta \mathrm{Fr} \lesssim \delta_{2c} \mathrm{Fr}$. Corresponding parameters are (a) $\delta \mathrm{Fr} = 3.89 \times 10^{-4}$, $\omega = 95.0$, and $R = 4778$, (b) $\delta \mathrm{Fr} = 3.88 \times 10^{-4}$, $\omega = 95.1$, and $R = 4907$, (c) $\delta \mathrm{Fr} = 3.88 \times 10^{-4}$, $\omega = 95.0$, and $R = 5389$, and (d) $\delta \mathrm{Fr} = 3.73 \times 10^{-4}$, $\omega = 96.7$, and $R = 6267$.

FIG. 9. Integrals of the power spectrum magnitude (arbitrary units) in the total power spectra ($\square$), harmonic wave-number band ($\bigcirc$), and subharmonic wave-number band ($\triangle$) depending on S_{2c} [Eq. (4)] for $\delta \mathrm{Fr} \lesssim \delta_{2c} \mathrm{Fr}$. Solid symbols denote the presence of a SQC pattern. Observed patterns at four representative parameter values are shown. The dotted lines are the corresponding values of S_{2c}. Larger versions of these patterns may be found in Fig. 8. Solid lines show fits of the open symbol data using the least squares method. Solid symbols are not used in the least squares fits and suggest (see text) interactions between stimulated length scales.

As a representative example for the pattern evolution near bicriticality observed in the experiments we will describe the transition that occurs at $\omega \approx 95$ and fixed $\delta \mathrm{Fr} \lesssim \delta_{2c} \mathrm{Fr}$. Initially the system is in a state of conduction with $R < R_{2c} \approx 4565$. Slowly increasing R (to $R \approx 4780$), small localized regions of subharmonic stripes occur on the harmonic hexagons [Fig. 8(a)] bifurcating at threshold. Further increasing R (to $R \approx 4900$), the subharmonic stripes begin to appear throughout the whole pattern superimposed on a mixed harmonic hexagon-stripe state [Fig. 8(b)]. Continuing into the coexistence parameter region, harmonic hexagons become less pronounced as patterns with domains of locally hexagonal, square, and rhombic symmetries begin to form [Fig. 8(c)], similar to those first reported in Ref. [22]. Eventually ($R \gtrsim 6270$), the harmonic component displays mainly domains of locally square symmetry [Fig. 8(d)] from which eventually regular SQCs emerge via an abrupt transition.

Changes in the experimental power spectra are observed as parameter values are varied to move the system from conduction to the SQC state. As shown in Fig. 5(a), the parameter region of SQC states tends toward smaller $\delta \mathrm{Fr}$ with increasing R. Thereby, beginning from a stable conductive state in the vicinity of the bicritical point R is increased while $\delta \mathrm{Fr}$ is slowly decreased. At a given ω the bicritical point $(\delta_{2c} \mathrm{Fr}, R_{2c})$ may be used to define a measure of distance into the coexistence region given by

$$S_{2c} = \frac{1}{\sqrt{2}} \left[\left(\frac{\delta \mathrm{Fr}}{\delta_{2c} \mathrm{Fr}} - 1 \right)^2 + \left(\frac{R}{R_{2c}} - 1 \right)^2 \right]^{1/2}. \quad (4)$$

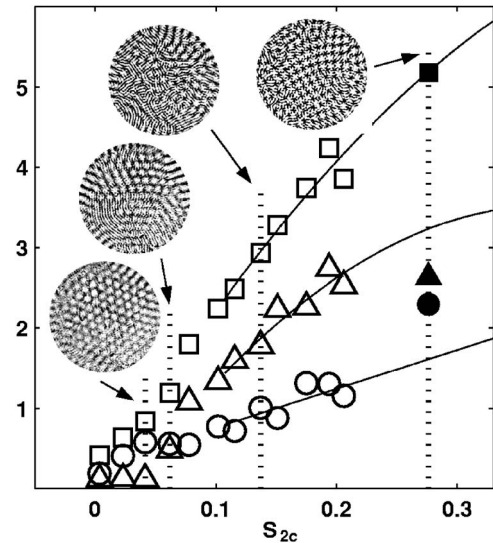Experiments following the described path find the total spectral power in the two-dimensional wave-number domain in-creases continuously as the system moves from conduction into coexistence states (Fig. 9). The presence of harmonic hexagons near the transition from conduction suggests the bifurcation is subcritical; however, the subcriticality is also expected to be difficult to detect [2]. Consistent with this expectation experiments find no hysteresis in the total spectral power. Since the harmonic and subharmonic contributions to coexistence patterns occur at distinct wave numbers, the spectral power in each may also be determined by summing the power in distinct wave-number bands centered on q^H and q^S (Fig. 9). As S_{2c} is slowly increased, moving the experiment into the parameter range of coexisting patterns, the spectral power for the q^H and q^S bands smoothly increase, with the power in the q^S band larger than the power in the q^H band. However, at the onset of the SQC state ($S_{2c} \approx 0.3$) the power distribution shifts abruptly as the q^H band power increases and the q^S band power decreases so both bands contain approximately equal power (solid symbols in Fig. 9). This shift is always observed at the onset of complex-ordered states and is suggestive of increased interactions between the q^H and q^S wave vectors.

B. Transition from pure harmonics

Beginning from a state of purely harmonic resonant convection and sufficiently large R, there is a well-defined transition to SQCs as $\delta \mathrm{Fr}$ is increased (Fig. 5). In the state of purely harmonic convection the pattern typically consists of parallel stripes with defects, including disclinations, dislocations, and foci [Fig. 10(a)]. With increasing $\delta \mathrm{Fr}$ at constant
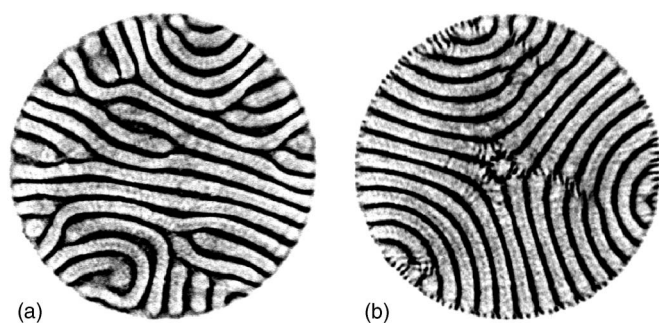
FIG. 10. Patterns (*experiment*) on either side of the purely harmonic-coexistence boundary. Pure harmonic stripes (a) with defects (δFr$=3.31\times10^{-4}$, $\omega=98.0$, $R=6280$). Coexistence state (b) with 3-foci harmonic stripes and subharmonic stripe patches (δFr $=3.54\times10^{-4}$, $\omega=98.0$, $R=6280$).

R, localized domains of subharmonic stripes emerge with a characteristic wave number q^S slightly less than $3q^H$. As can be seen in Fig. 10(b) these subharmonic domains are usually either centered about defects in the harmonic pattern or aligned perpendicular to the lateral boundaries. Subharmonic stripes at the lateral boundary typically remain pinned to the boundary and do not move into the interior. Harmonic defects continually nucleate, become advected, and annihilate in the pattern interior. These persistent dynamics drive the behavior of the subharmonic patches, which correspondingly appear, move, and disappear. Although harmonic defects are virtually always present for parameter values near the harmonic-subharmonic coexistence boundary, not all these harmonic defects have associated subharmonic patches. As a result the subharmonic components are intermittent in time near coexistence onset for a range of δFr of width $\approx4\times10^{-6}$. The subharmonic onset is difficult to detect in power spectra because spatial and temporal intermittency gives rise to a small spectral component that is nearly indistinguishable from background noise and the second harmonic of q^H [compare Fig. 11(a) and Fig. 11(b)]. The transition is more reliably identified using the real space patterns. Thus the onset value of δFr for a given R is defined as the presence of subharmonic patches in the pattern interior for at least 10% of the observation time.

The experimentally measured boundary for the emergence of subharmonic convection when harmonic convection is already established follows the subharmonic marginal stability curve (dashed in Fig. 12). The observed shift indicates the bifurcation of subharmonic modes, though their linear growth rate is already positive, is delayed by their interaction with the finite amplitude harmonic pattern. However, in the cores of defects this stabilizing mechanism is reduced due to smaller harmonic flow amplitudes [33]. Thereby subharmonic patches associated with harmonic defects are a precursor to the coexistence transition in the pattern bulk.

In the parameter region between coexistence onset and the formation of SQCs, patterns display gradual changes. From inspection of the patterns the subharmonic component remains spatially localized and intermittent even as δFr is increased (at fixed R) to move the system well away from the pure harmonic-coexistence boundary (Fig. 12). The spectral
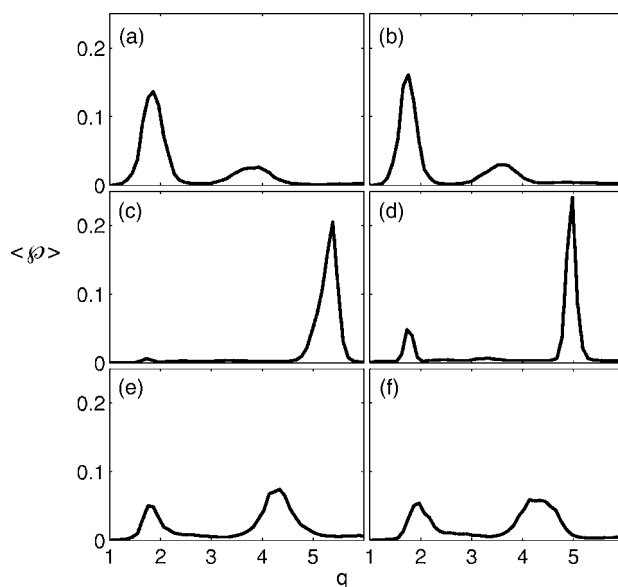

FIG. 11. Averaged radial power spectra (*experiment*) for three different transitions to coexistence with local maxima near $q=q^H$ and $q=q^S>q^H$. Each radial spectrum shown is the average over 40 spectra computed from the spatial images recorded at each set of parameters. Pure harmonic-coexistence [(a) and (b)] transition occurring at $R=6280$. The pure subharmonic-coexistence transitions occurring at $R=4980$ [(c) and (d)] and well-developed coexistence patterns at $R=6280$ [(e) and (f)]. Representative images from each data point are shown in other figures, (a) see Fig. 10(a), (b) see Fig. 10(b), (c) see Fig. 14(a), (d) see Fig. 14(b), (e) see Fig. 14(c), and (f) see Fig. 14(d).

contribution of the subharmonic pattern component, shown in Fig. 13(a), gradually increases with increasing δFr. Over this parameter range the wave number of harmonic modes q^H remains relatively fixed [Fig. 13(b)]. Additionally, the spectral width σ^H decreases [Fig. 13(c)] because the harmonic pattern exhibits fewer defects as the system moves further away from the pure harmonic-coexistence boundary.

Moving further into coexistence by increasing δFr, the transition to SQCs from the mostly harmonic patterns containing localized subharmonics is abrupt. Just prior to this transition there is a pronounced increase in the subharmonic component in patterns. Typically this transition occurs over a relatively narrow range of δFr($\sim5\times10^{-6}$) and corresponds to the harmonic planforms separating into multiple domains. At the transition, the harmonic modes contain $\sim60\%$ of the total power and values of q^H and σ^H (Fig. 13) attain minimums. In contrast, the wave number of the subharmonic modes q^S is near its maximum observed value. Simulations of the Boussinesq equations at these relatively large values of R predict well the transition from localized coexistence patterns to SQCs [Fig. 5(a)]. This result indicates that non-Boussinesq effects play an insignificant role in the formation of complex-ordered patterns further away from the bicritical point.

C. Transition from pure subharmonics

The evolution of purely subharmonic convection patterns with decreasing δFr exhibits a sequence of coexisting pat-
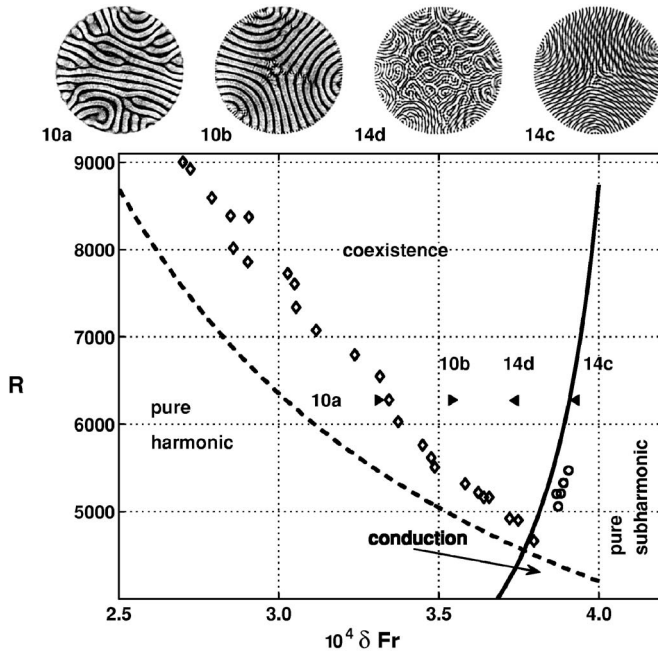
FIG. 12. Phase plane ($\omega=98$) comparing the experimentally measured onset of coexistence to the linear marginal curves for conduction; see also Fig. 2. Boundary between coexistent and purely harmonic flows ($\diamond$) follows the marginal subharmonic ($\omega/2$) curve (dashed line), while the boundary between coexistent and purely subharmonic patterns ($\bigcirc$) tracks the marginal harmonic (ω) curve as far as the boundary can be reliably determined. Solid triangles are the locations of patterns in Figs. 10(a), 10(b), 14(c), and 14(d), also shown along the top row as indicated.

terns that are qualitatively different from those observed in the transition from pure harmonic side (see Sec. III B). Pure subharmonic patterns lose stability to coexisting states as the harmonic component emerges globally; no localized harmonics are observed. For $\omega=98.0$ we will distinguish two cases, (1) $R_{2c}<R<5500$ and (2) $R>5500$. The experiments do not observe a transition to SQCs in case (1), in contrast to the simulations, while in case (2) both experiments and simulations find a transition to SQCs.

Approaching the coexistence region starting from pure subharmonic parallel stripes [Fig. 14(a)] by slowly decreasing δFr at fixed R for $R_{2c}<R\lesssim5500$ [case (1)] a harmonic pattern component emerges at a well-defined location in parameter space and begins to be present throughout the pattern. For instance in Fig. 14(b) the weak harmonic stripes rising from left to right at an angle of approximately 30° to the horizontal and possessing a wavelength about 3 times that of the prevalent subharmonic stripes are clearly visible.

Although the harmonic component is weak at the pure subharmonic-coexistence onset, the transition is well defined and readily detectable in Fourier space by looking for the initial presence of power at q^H [Figs. 11(c) and 11(d)]. Typically, the emerging harmonic component consists of fairly large patches of parallel stripes which may display domains with several orientations. In this parameter range, the coexistence transition is well predicted by the *conduction* marginal stability curve solid line in Fig. 12, suggesting that in contrast to the transition described in Sec. III B the onset of

bifurcating mode (harmonic convection) is, loosely speaking, neither enhanced or suppressed through the interaction with already existing finite amplitude subharmonic flows. Hysteresis is not experimentally observed in the transition between pure subharmonic flows and the coexistence regime.

For $R\gtrsim5500$ [case (2)] the coexistence states compete with more complex pure subharmonic flows. For $5500\lesssim R\lesssim7000$, subharmonics with transverse modulations [Fig. 14(c)] are found when δFr is relatively large (Fig. 12). As δFr is decreased at constant R and crosses the conduction marginal stability boundary, the flow structure changes gradually to patterns like that shown in Fig. 14(d). In all cases, these states are difficult to distinguish spectrally because they contain spectral peaks with similar power content at wave numbers corresponding to both q^S and q^H [Figs. 11(e) and 11(f)]. As a result, the onset of the coexistence regime from pure subharmonics is ill defined for $R>5500$. At even larger R ($R>7000$) patterns display no clear spatial structure, instead showing regions of varying shadowgraph intensities consisting of plume structures (not shown). For $R\gtrsim7000$ the structurally disordered state becomes more ordered with decreasing δFr.

Spectral analysis demonstrates that the gradual nature of the transition from pure subharmonics to coexisting patterns continues as δFr is further decreased. For $R\lesssim5500$ the growing harmonic stripes have little effect on the subharmonic stripes as the two components are simply superimposed. For $5500\lesssim R\lesssim7000$ the subharmonic striped base state that supports the transverse modulations gradually breaks down as numerous domains form [Figs. 14(c) and 14(d)]. Typically, these domains nucleate in the pattern interior and spread to fill the pattern with decreasing δFr. Regardless of the R value the spectral measures display similar trends. First, relative power in $\wp^S$ gradually decreases and $\wp^H$ slowly increases as the harmonic pattern becomes more significant [Fig. 13(a)]. Second, q^H [Fig. 13(b)] remains relatively fixed while σ^H decreases [Fig. 13(c)]. Simultaneously, q^S slowly increases while σ^S remains relatively constant. These similarities indicate that as the pattern passes further into coexistence the harmonic pattern slowly grows and becomes more regular while $\wp^S$ slowly decreases and q^S increases.

Upon further decreases of δFr, the subharmonic dominated coexistence patterns abruptly lose stability to SQC patterns. At this transition, the subharmonic modes contain $\approx60\%$ of the total power. Experimental investigations observe no hysteresis in the formation of SQCs. The formation time for a single cell-filling domain of harmonic squares in an SQC state becomes substantially larger near the transition boundaries with both harmonic dominated and subharmonic dominated coexistence patterns. Simulations of the Boussinesq equations at these large values of R agree with the transition from subharmonic dominated coexistence patterns to SQCs. A comparison for a particular value of R is shown in Fig. 5(a). These observations further support that non-Boussinesq effects play an insignificant role in the formation of complex-ordered patterns further away from the bicritical point.
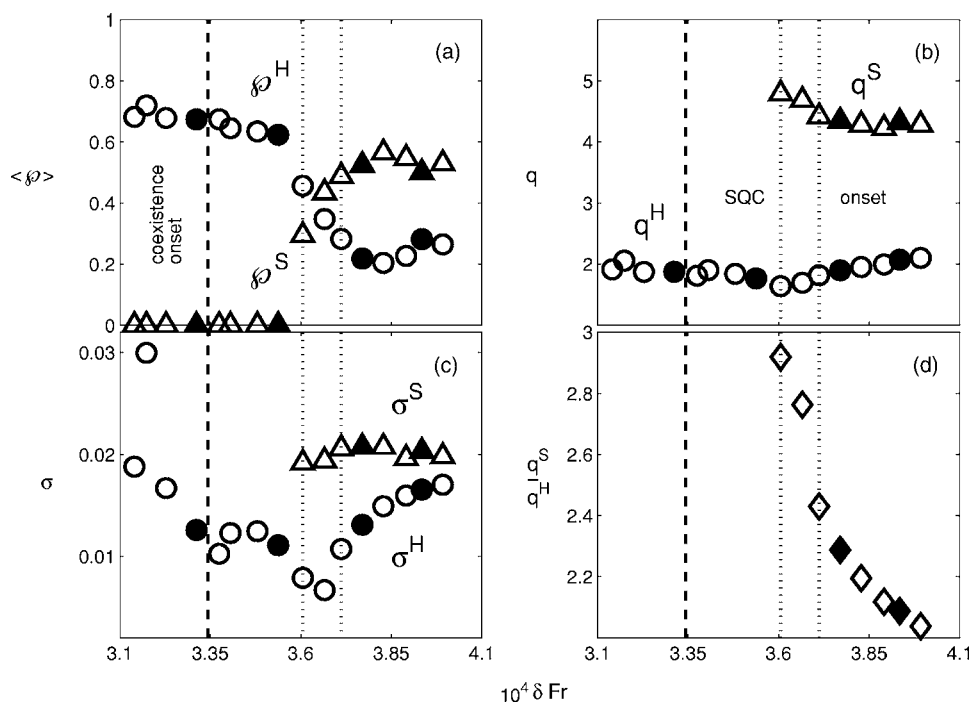
FIG. 13. Spectral quantities during the transition (*experiment*) from pure harmonic convection to pure subharmonic convection through a coexistence region. Experiments pass through coexistence by increasing δFr at $R = 6280 \pm 10$. Each radial spectrum used to calculate these quantities is an average over 40 spectra computed from the images recorded at each set of parameters. The averaged radial spectra for both the harmonic and subharmonic modes are characterized by (a) the spectral power in each mode—$\wp^H$ and $\wp^S$, (b) the mode wave numbers—q^H and q^S, (c) the widths of the spectral peaks—σ^H and σ^S, and (d) the wave-number ratio q^S/q^H. Throughout, $\bigcirc$ indicates harmonic pattern component and $\triangle$ the subharmonic pattern component. Filled in symbols correspond to patterns shown in Figs. 10(a), 10(b), 14(c), and 14(d). The dashed lines are the boundaries of coexistence and the dotted lines are the boundaries of SQCs.

FIG. 14. Patterns (*experiment*) on either side of the pure subharmonic-coexistence transition ($\omega = 98.0$) for $R = 4980$ [(a) δFr$= 3.80 \times 10^{-4}$ and (b) δFr$= 3.69 \times 10^{-4}$] and $R = 6280$ [(c) δFr $= 3.93 \times 10^{-4}$ and (d) δFr$= 3.77 \times 10^{-4}$].

IV. RESONANT TETRADS

Analysis of power spectra for the observed complex patterns demonstrate that these states are described by a few interacting spectral modes and generally form a quasiperiodic crystals. SQCs (Fig. 4) have spectra with twelve dominant peaks in two distinct wave number bands, as shown in Fig. 15(a). The four peaks $\pm(\mathbf{q}_1^H, \mathbf{q}_2^H)$ correspond to the harmonic square sublattice. The eight peaks $\pm(\mathbf{q}_1^S, \mathbf{q}_2^S, \mathbf{q}_3^S, \mathbf{q}_4^S)$ correspond to the small length scale subharmonic stars [Fig. 4(a)]. The stripe superlattices [Fig. 6(a)] exhibit six dominant peaks. The harmonic stripe sublattice corresponds to the two peaks at $\pm\mathbf{q}_1^H$ while subharmonic sublattice corresponds to peaks at $\pm(\mathbf{q}_1^S, \mathbf{q}_2^S)$.

Interactions between the modes from the harmonic and subharmonic sublattices are found to satisfy resonance conditions. The spectral peaks for SQCs form the vertices of parallelograms between a pair of the harmonic and a pair of the subharmonic peaks [Fig. 15(a)]. Existence of these parallelograms suggests the four wave resonance (*resonant tetrad*) conditions,

$$\pm(\mathbf{q}_1^H - \mathbf{q}_2^H) = \pm(\mathbf{q}_1^S - \mathbf{q}_2^S), \quad (5)$$

$$\pm(\mathbf{q}_1^H + \mathbf{q}_2^H) = \pm(\mathbf{q}_3^S - \mathbf{q}_4^S). \quad (6)$$

In both experiments and numerics SQCs always satisfy these resonant tetrad conditions. In the vicinity of the bicritical point the parallelograms formed by the modes become rect-
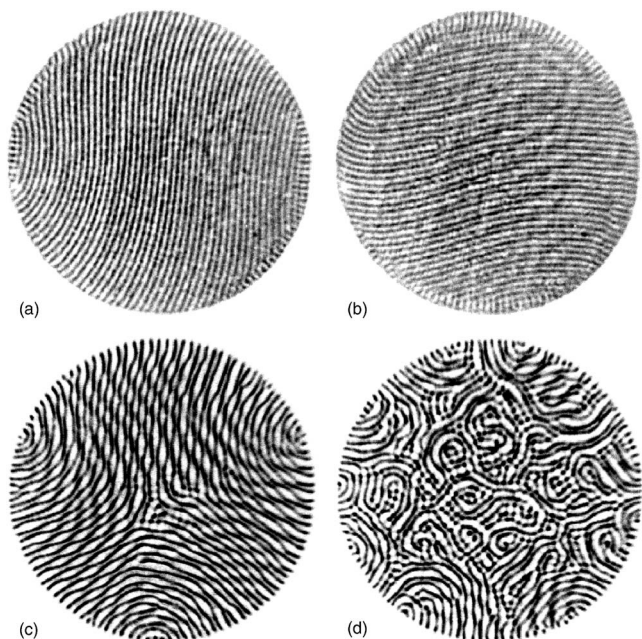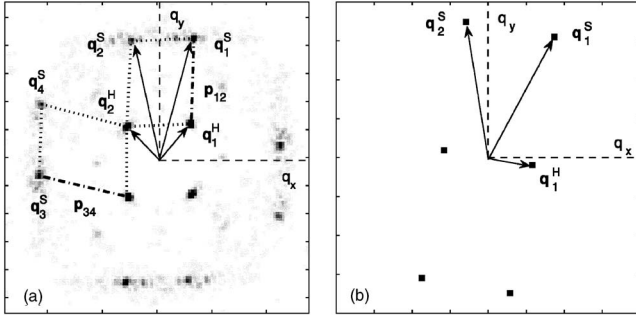
FIG. 15. Power spectra for: (a) the SQL in Fig. 4(a) and (b) the stripe superlattice shown in Fig. 6(a). Arrows point to modes comprising a resonant tetrad, these are emphasized by the dotted and dotted-dashed lines. The dotted-dashed lines are difference vectors defined in Eqs. (21)

angles. Further from onset, subharmonic spectral peaks translate short distances along the straight lines formed by the box passing through the eight subharmonic peaks allowing the $|\mathbf{q}_i^S|$ ($i=1,\ldots,4$) to take on different values for all i, while always satisfying Eqs. (5) and (6). Experiments indicate that with increasing R the SQC wave vectors have relatively constant q^H ($0.91q_{2c}^H \lesssim q^H \lesssim 0.94q_{2c}^H$) and that q^S decreases monotonically from $0.92q_{2c}^S$ at $R=6280$ to $0.77q_{2c}^S$ at $R=8920$. A four wave resonance condition also applies for the stripe superlattices; in this case, the condition is given by

$$\pm 2\mathbf{q}_1^H = \pm(\mathbf{q}_1^S - \mathbf{q}_2^S). \qquad (7)$$

This resonance condition is a tetrad between modes at q^H and q^S with a self-interaction term for the harmonic mode [Fig. 15(b)].

The noted prominence of the 12 modes satisfying resonant tetrad conditions [Eqs. (5) and (6)] suggests the SQCs may be represented using the ansatz of an eigenmode expansion in the spirit of a weakly nonlinear analysis. We represent the temperature field Θ and velocity field $\mathbf{v}$ (Sec. II B) as a symbolic vector $\mathbf{V}(\mathbf{x},z,t)=(\Theta(\mathbf{x},z,t),\mathbf{v})$. The shadowgraph intensity reflects the horizontal variations of $\Theta(\mathbf{x},z,t)$ [29]. Linear stability analysis of Eqs. (3) yield the linear eigenvectors $\mathbf{V}^{H,S}(\mathbf{q},z,t)$ and the corresponding growth rates $\lambda_{H,S}(\mathbf{q},R)$ for the harmonic and subharmonic responses, respectively. Above the corresponding threshold curves (Sec. I) the real part of the growth rates become positive. The time dependence of the harmonic and subharmonic eigenmodes (V^H and V^S) is given by Floquet's theorem,

$$V^{H,S}(\mathbf{q},z,t) = \mathrm{Re}\left(e^{t\mu^{H,S}} \sum_{n=-\infty}^{\infty} \mathbf{c}_n^{H,S}(\mathbf{q},z)e^{in\omega t} \right), \qquad (8)$$

normalized such that $|\mathbf{c}_0^{H,S}(\mathbf{q},z{=}0)|=1$ with Floquet exponents $\mu^H=0$ for harmonic modes and $\mu^S=i\omega/2$ for subharmonic modes. Since the mode V^H is essentially sinusoidal about nonzero mean, only the first two terms ($n=0$ and $n\pm 1$) need to be retained. In contrast, V^S requires at least three harmonics ($n=\pm 1, \pm 3, \pm 5$) of $\omega/2$. In the framework of the weakly nonlinear reformulation, the ansatz for ideal SQC is

$$\mathbf{V}(\mathbf{x},z,t) = \mathrm{Re}\left(\sum_{j=1}^{2} A_j(t)\mathbf{V}^H(\mathbf{q}_j^H,z,t)e^{i\mathbf{q}_j^H \cdot \mathbf{x}} \right)$$
$$+ \mathrm{Re}\left(\sum_{j=1}^{4} B_j(t)\mathbf{V}^S(\mathbf{q}_j^S,z,t)e^{i\mathbf{q}_j^S \cdot \mathbf{x}} \right). \qquad (9)$$

Inserting Eq. (9) into the Boussinesq equations and systematically expanding in terms of the amplitudes, which are small near onset, up to cubic order produces coupled amplitude equations for A and B given by

$$\frac{d}{dt}A_1 = \lambda_H(\mathbf{q}_1^H)A_1 + \gamma_1 A_1 + \eta_{11}A_2 B_1 B_2^* + \eta_{12}A_2^* B_3 B_4^*,$$

$$\frac{d}{dt}A_2 = \lambda_H(\mathbf{q}_2^H)A_2 + \gamma_2 A_2 + \eta_{21}A_1 B_2 B_1^* + \eta_{22}A_1^* B_3 B_4^*,$$

$$\frac{d}{dt}B_1 = \lambda_S(\mathbf{q}_1^S)B_1 + \gamma_3 B_1 + \eta_{31}B_2 A_1 A_2. \qquad (10)$$

The standard cubic terms with coupling constants c_{ij} are

$$\gamma_j = c_{1j}|A_1|^2 + c_{2j}|A_2|^2 + c_{3j}|B_1|^2 + c_{4j}|B_2|^2 + c_{5j}|B_3|^2$$
$$+ c_{6j}|B_4|^2. \qquad (11)$$

The resonant mode interactions are given by the terms $\sim A_2 B_1(B_2)^*$, $(A_2)^* B_3(B_4)^*$, etc., with coupling constants η_{ij} that are the strengths of the interactions. The remaining equations for the amplitudes B_j in Eq. (9) are obtained by cyclic permutations of the indices. Note that the presence of Boussinesq symmetry invariance under spatial inversion rules out quadratic couplings.

We have calculated the coefficients c_{jj} ($j=1,\ldots,6$), which determine the saturation of the amplitudes A_j and B_j. They were always positive, consistent with the observed supercritical bifurcation of both the harmonic and subharmonic rolls at threshold. The tedious calculation of the cross coefficients which govern the stability of the SQCs and the values of the finite amplitudes A and B has not been carried through. Instead we have confirmed the relevance of the amplitude equations (10) by extracting the amplitudes from numerical simulations of SQCs by the suitable projections with the eigenmodes V^H, V^S. In fact, to represent a snapshot of a SQC where the spectral peaks form rectangles [Fig. 4(b)] only two constant real amplitudes, A and B with $A=A_1 =-A_2, B=B_1=B_2=B_3=B_4$, are required by Eq. (9). It turns out that the time evolution of the SQCs is described by $AV^H(t)$ and $BV^S(t)$ with adjusted amplitudes A and B (Fig. 16). For fixed Pr, $\delta \mathrm{Fr}=\delta_{2c}\mathrm{Fr}$, and ω the amplitudes increased proportionally to the square root $\sqrt{(R-R_{2c})}$ of the distance from onset, confirming the forward bifurcation.

Although we have not calculated all coefficients in Eq. (10) it is possible to reveal some general properties of the solutions A and B. Initially, we find it useful to characterize the complex amplitudes by their moduli and phases,

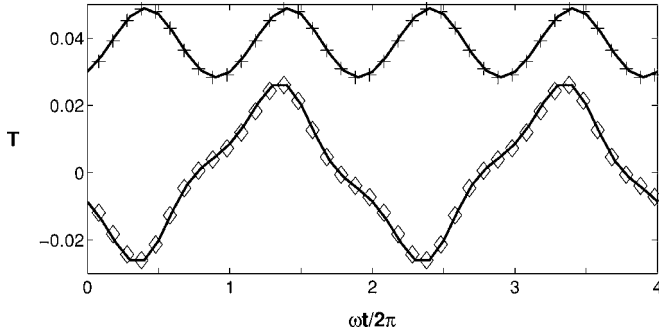$$A_j = |A_j|\exp(i\phi_j), \quad j=1,2,$$

FIG. 16. The temporal variation (*simulation*) of linear eigenvectors multiplied with adjusted amplitude factors $A=0.0382$, $B=0.0108$ (see text) at $\delta \mathrm{Fr}=3.732 \times 10^{-4}$, $R=4790$ for the harmonic (upper curve) and subharmonic (lower curve) modes, respectively. Comparison is made with the numerical amplitudes of the Fourier modes at $\mathbf{q}_1^H$ (+) and $\mathbf{q}_1^S$ ($\diamond$), respectively, for the SQC midplane temperature field $T(\mathbf{x},t) \equiv \Theta(\mathbf{x},z=1/2,t)$ in units of ΔT.

$$B_k = |B_k| \exp(i\psi_k), \quad k=1,\ldots,4. \qquad (12)$$

The amplitudes and phases can be easily extracted from our numerical solutions by projecting the solutions on the linear eigenvectors $\mathbf{V}^{S,H}(\mathbf{q},z,t)$. Due to the invariance against translations in the plane, patterns are in fact physically equivalent, if their phases differ by certain shifts $\delta\phi_i$ and $\delta\psi_i$, obeying the constraints

$$\delta\phi_1 - \delta\phi_2 = \delta\psi_1 - \delta\psi_2,$$

$$\delta\phi_1 + \delta\phi_2 = \delta\psi_3 - \delta\psi_4. \qquad (13)$$

This invariance property is also directly reflected in the amplitude equations. In all simulations we found the following relations hold:

$$\phi_1 - \phi_2 + n\pi = \psi_1 - \psi_2,$$

$$\phi_1 + \phi_2 - n\pi = \psi_3 - \psi_4, \qquad (14)$$

for arbitrary odd integers n. This relation expresses the resonance between the harmonic and subharmonic modes. For definiteness we can always fix the harmonic phases to $\phi_1 = 0$ and $\phi_2 = \pi$. Since only two conditions are left to determine the four subharmonic phases, two of them remain undetermined in the framework of Eqs. (10). This freedom can be interpreted as a shift of the short wavelength structures due to the four subharmonic modes relative to the harmonic backbone lattice. There should exist a locking mechanism as a result of nonlinear couplings, automatically included in the Boussinesq equations, at orders beyond the cubic in the amplitude equations. However, in addition to the conceptual difficulty described in Ref. [34] such calculations are cumbersome [35] and thereby beyond the scope of this paper. Simulations using random initial conditions always lock into a stationary set of phases; however different runs yield different sets of phases for fixed external parameters (Pr, R, δFr, and ω). We have been unable to classify these further, in particular since the corresponding patterns look practically identical. The subharmonic phases are expected to present a

soft degree of freedom, easily susceptible to all kinds of small perturbations (for example, boundary effects).

We have not performed a detailed investigation of the analogous coupled amplitude equations for the stripe superlattice [Fig. 6(a)]; these contain a resonant coupling $\sim (A)^* B_1 (B_2)^*$. The stripe superlattices can be described analogously by Eq. (9) with one harmonic amplitude A and two subharmonic amplitudes $B_{1,2}$, where $B_1 = B_2 = iB$.

In the non-Boussinesq experiments and numerics, harmonic hexagonal background patterns observed in the vicinity of the bicritical point would delay the onset of SQCs. In this case, quadratic couplings in the amplitude equations are allowed between the harmonic modes, while quadratic couplings remain forbidden between the subharmonic modes due to the temporal symmetry. In the case of a hexagonal backbone, we must consider the presence of three harmonic basis wave vectors $\mathbf{p}_i$ ($i=1,2,3$) ($|\mathbf{p}_i|=q^H$) satisfying the constraint that the basis vectors sum to zero ($\mathbf{p}_1 + \mathbf{p}_2 + \mathbf{p}_3 = \mathbf{0}$). We have not investigated in detail the possibility of resonant couplings to the subharmonic modes, which according to Fig. 8 should exist.

V. OTHER COMPLEX-ORDERED PATTERNS

Preliminary experimental and numerical investigations demonstrate that a wide variety of quasiperiodic crystals and superlattices, all governed by resonant tetrads, exist in the current system. Due to the resonance conditions the spatial structure of these patterns is mainly determined by the ratio $q^S/q^H > 1$, which depends sensitively on ω through the ratio of wave numbers at bicriticality $q^S/q^H \approx q_{2c}^S/q_{2c}^H$. A different group of wave-number ratios ($q^S/q^H < 1$), that also depend sensitively on ω, exist when the system is heated from above ($R<0$). Several representative examples of variations in complex order are shown below.

A. Heating from below

When the convection cell is heated from below $R>0$ we find a range of complex-ordered patterns. Examples are shown for $\omega=40$ in Fig. 17(a) and $\omega=300$ in Fig. 17(b). These complex-ordered patterns are qualitatively similar to those observed at $\omega \approx 100$ due to the harmonic component forming a regular square sublattice on which the subharmonic structures exist. However, the subharmonic small scale component of these patterns becomes more complex with increasing ω. At $\omega=40$ SQCs with subharmonic crosses form with $q^S/q^H=2.236$, at $\omega \approx 100$, $q^S/q^H=2.912$ one sees stars with more spikes, while at $\omega=300$ with $q^S/q^H=5.42$ one observes well ordered multispike stars.

All these complex-ordered patterns satisfy similar resonant tetrad conditions. The patterns for $\omega=40$ and $\omega \approx 100$ present only quantitative differences in their spectral structure [Figs. 4(c) and 17(c)] consistent with the tetrad conditions in Eqs. (5) and (6). At $\omega=300$ the spectral structure changes as six pairs of peaks now span the subharmonic component. This SQC satisfies a kind of "duplicated" resonant tetrad condition compared to Eqs. (5) and (6),
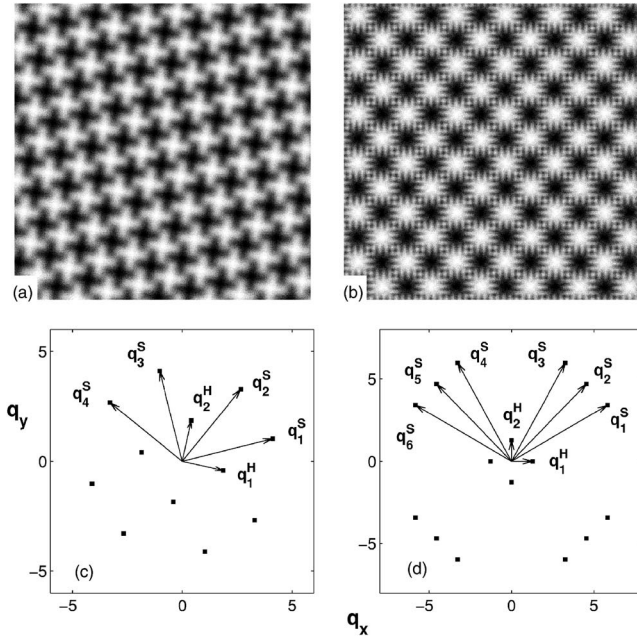
FIG. 17. Complex-ordered patterns (*Boussinesq simulation*) observed at other oscillation frequencies. At $\omega=40$ (a) regular subharmonic crosses on a square harmonic sublattice are observed ($\delta\mathrm{Fr}=12.375\times10^{-4}$ and $R=4000$), while at $\omega=300$ (b) the subharmonic component forms multispike stars ($\delta\mathrm{Fr}=1.167\times10^{-4}$ and $R=7800$). The pattern in (a) has the same spectral structure (c) as the SQCs [Figs. 4(c) and 4(d)]. In contrast, the pattern in (b) has a power spectrum (d) with 12 subharmonic peaks.

$$\pm(\mathbf{q}_1^H-\mathbf{q}_2^H)=\pm(\mathbf{q}_2^S-\mathbf{q}_1^S)=\pm(\mathbf{q}_3^S-\mathbf{q}_2^S), \qquad (15)$$

$$\pm(\mathbf{q}_1^H+\mathbf{q}_2^H)=\pm(\mathbf{q}_5^S-\mathbf{q}_6^S)=\pm(\mathbf{q}_4^S-\mathbf{q}_5^S). \qquad (16)$$

A qualitatively different rhombic quasiperiodic crystal (RQC) is found in both experiments and simulations [Figs. 18(a) and 18(b)] when ω is sufficiently small. For RQCs the harmonic and subharmonic sublattices are defined by two pairs of spectral peaks, while the SQC subharmonic sublattice has four pairs of peaks. [Compare Figs. 15(a), 18(c), and 18(d).] The RQCs also satisfy one of the resonant tetrad conditions [Eq. (5)] found earlier for SQCs. Experiments find RQCs at $\omega=50$ with $q^S/q^H=2.23$, in contrast to the simulations, which showed quasiperiodic crystals qualitatively similar to those studied more extensively at $\omega=98$, but with a smaller wave-number ratio $q^S/q^H=2.24$. In the simulations it was necessary to reduce the oscillation frequency to below $\omega=40$, to identify RQCs as shown for $q^S/q^H=2.08$. The reasons for the discrepancies in parameter values between experiment and simulations for RQCs have not been investigated in detail, but a competition of the SQC and RQC attractors in a certain ω range may well exist.

B. Heating from above

Simulations of the qualitatively different case of adding heat to the convection cell from the top plate ($R<0$) also find complex-ordered patterns (Fig. 19). Our investigations of heating from above are restricted to numerical simula-
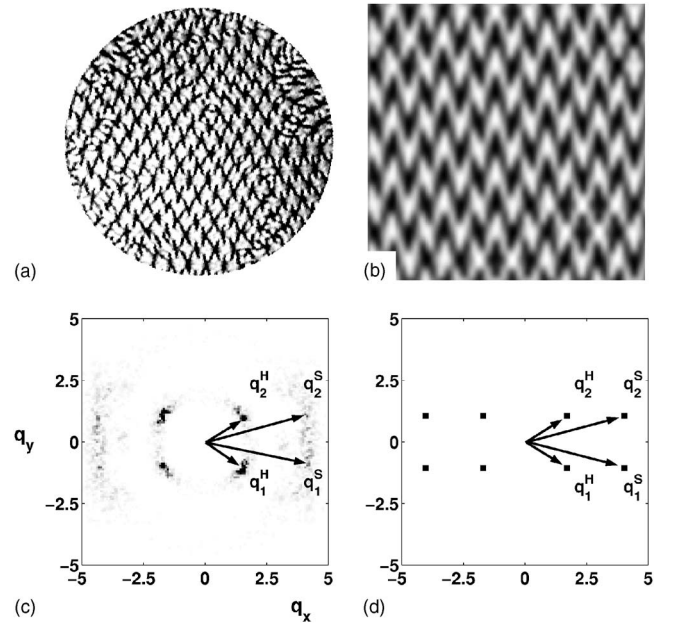

FIG. 18. Rhombic quasiperiodic crystals observed in experiments (a) and Boussinesq simulations (b). Corresponding power spectra are shown in (c) and (d), respectively. Parameters values are experiment $\mathrm{Pr}=0.928$, $\delta\mathrm{Fr}=8.92\times10^{-4}$, $\omega=50.4$, $R=5180$ and simulations $\mathrm{Pr}=0.930$, $\delta\mathrm{Fr}=16.74\times10^{-4}$, $\omega=33$, $R=3800$.

tions. In contrast to the heating from above case, the onset subharmonic wave numbers are smaller than the harmonic ones ($q_c^S<q_c^H$). Critical Rayleigh numbers and critical wave numbers are presented in Figs. 2(c) and 2(d), respectively. Looking in the vicinity of the bicritical points we again find complex-ordered patterns. While SQCs are not yet found in this case, a state [Fig. 19(a)] that is qualitatively similar to the stripe superlattices [Fig. 6(a)] is observed. The wave-number ratio of this pattern is $q_j^S/q_j^H=0.479$.

The corresponding resonant tetrad condition takes a form,

$$\pm2\mathbf{q}_1^S=\pm(\mathbf{q}_1^H-\mathbf{q}_2^H), \qquad (17)$$

identical to Eq. (7) with the transposition $(S\to H, H\to S)$.

VI. CLASSIFYING COMPLEX ORDER

Complex-ordered patterns reported in Secs. III and V and designated as quasiperiodic crystals or superlattices may be
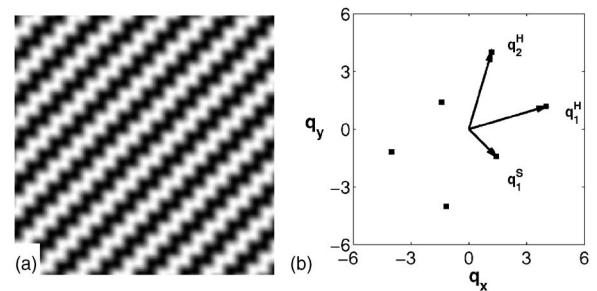

FIG. 19. Stripe superlattice (*Boussinesq simulation*) observed with heating from above (a) at $\delta\mathrm{Fr}=25.2\times10^{-4}$, $\omega=50$, $R=-2800$. Corresponding power spectrum (b).

distinguished on the basis of periodicity. All of the observed patterns are found to be characterized in Fourier (**q**) space by relatively few wave vectors. These wave vectors are grouped in two distinct classes based on magnitudes and form parallelograms satisfying the appropriate resonant tetrad conditions. Due to the prominence of the longer length scale (smaller q) sublattice, the reported states display an obvious regularity in position space (i.e., square, hexagonal, or rhombic). Defining appropriate linear combinations of the dominant wave vectors, the requirements for the observed spatial regularity to be periodic can be formulated. These requirements permit a general classification of the patterns on the basis of concepts formulated in crystallography.

For clarity we briefly restate relevant definitions of Ref. [9], where Lifshitz proposes nomenclature for patterns characterized in Fourier space by a countable set of L wave vectors. The set L (i.e., Fourier module) consists of integral linear combinations of a minimum number D of basic wave vectors $\mathbf{q}_i$ $(i=1,\ldots,D)$. If D is greater than the physical dimension d of the pattern (two, in the present case) the state is called a *quasiperiodic crystal pattern*. In practice not all modes of L need to be excited and typically only a few dominant ones determine the gross features of the pattern. In the case of $D=d$ the pattern is strictly periodic and is called a *superlattice pattern*. The Fourier module is then identical to the conventional reciprocal lattice in crystallography and two basis vectors $\mathbf{q}_i$ $(i=1,2)$ span a primitive unit cell in reciprocal space. The corresponding pattern is thus spatially periodic (translationally invariant) against all discrete translations formed by linear integral combinations of primitive basis vectors $\mathbf{a}_i$ $(i=1,2)$, that satisfy the conditions

$$\mathbf{q}_i \cdot \mathbf{a}_j = 2\pi\delta_{i,j} \quad (i,j=1,2). \tag{18}$$

To correlate these statements with the observed complex states consider the patterns shown in Figs. 4(a), 4(b), 17(a), and 17(b). Similar to the majority of states observed in these investigations the harmonic backbones are squares carrying stars at the lattice points. We name these states by the dominant regular structure; SQC patterns have a square backbone and RQC patterns have a rhombic backbone. The corresponding superlattice patterns $(D=d=2)$ are special cases that, despite their disparate length scales ($\sim 2\pi/q^H$ and $\sim 2\pi/q^S$, respectively), are spatially periodic.

For the SQCs, without lack of generality, the backbone square lattice derives from the two orthogonal basis vectors

$$\mathbf{q}_1^H = q^H(\cos(\alpha),\sin(\alpha)),$$

$$\mathbf{q}_2^H = q^H(-\sin(\alpha),\cos(\alpha)), \tag{19}$$

which for $\alpha=0$ would be aligned along the x and y axis, respectively. The basis vectors $\mathbf{a}_i^H$ of the ensuing Bravais lattice in position space, which are parallel to $\mathbf{q}_i^H$ are

$$\mathbf{a}_1^H = \frac{2\pi}{(q^H)^2}\mathbf{q}_1^H \quad \text{and} \quad \mathbf{a}_2^H = \frac{2\pi}{(q^H)^2}\mathbf{q}_2^H. \tag{20}$$

The lattice constant a^{SQ} of the square lattice is given by $a^{SQ}=2\pi/q^H$. The resonant tetrad conditions, Eqs. (5) and (6),

are guaranteed if the following ansatz for the subharmonic wave vectors $\mathbf{q}_i^S$ $(i=1,\ldots,4)$ is used:

$$\mathbf{q}_i^S = \mathbf{q}_i^H + \mathbf{p}_{12} \ (i=1,2),$$

$$\mathbf{q}_i^S = (-i)^{i-1}\mathbf{q}_{i-2}^H + \mathbf{p}_{34} \quad (i=3,4). \tag{21}$$

The vectors $\mathbf{p}_{ij}$ are shown in Fig. 15(a).

The special case of SQLs $(D=2)$ is realized if the $\mathbf{p}_{ij}$ can be represented as commensurate linear combinations of the harmonic vectors as

$$\mathbf{p}_{12} = C_1\mathbf{q}_1^H + C_2\mathbf{q}_2^H \quad \text{and} \quad \mathbf{p}_{34} = C_3\mathbf{q}_1^H - C_4\mathbf{q}_2^H, \tag{22}$$

where the coefficients $C_j=m_j/n_j$ $(j=1,\ldots,4)$ are rational numbers constructed from relative prime integers m_j, n_j. The SQL is then strictly periodic with respect to two basic translations

$$\mathbf{a}_i^{SL} = k_i\mathbf{a}_i^H \quad (i=1,2), \tag{23}$$

with k_1 the least common multiple of the integers n_1 and n_2 as well as k_2 the least common multiple of n_3 and n_4. [Note that as a consequence of $\mathbf{a}_i^{SL}\mathbf{q}_j^S=k_i2\pi\delta_{ij}$, all scalar products of the $\mathbf{a}_i^{SL}$ $(i=1,2)$ and the $\mathbf{q}_j^S$ $(j=1,\ldots,4)$ from Eqs. (21) and (22) give integer multiples of 2π]. Consistent with Eq. (18) the basic real space translations $\mathbf{a}_i^{SL}$ $(i=1,2)$ are associated with the shorter basis vectors $\mathbf{q}_i^H/k_i$ $(i=1,2)$ in Fourier (reciprocal) space. These are then consistent with the larger periodicity cell in position space [Eq. (23)].

The relationship between harmonic and subharmonic wave numbers is simplified when the SQL spectral parallelograms become rectangles [as in the numerical example in Fig. 4(d)]. In this case the constants $C_j=m_j/n_j$ become equal, i.e., $m_i=m$ $(i=1,\ldots,4)$ and $n_i=n$ $(i=1,\ldots,4)$. Then Eqs. (21) and (22) indicate that the wave vectors $\mathbf{q}_i^S$ $(i=1,\ldots,4)$ all have the same magnitude q^S. The vector $\mathbf{p}_{12}$ encloses an angle of 45° with $\mathbf{a}_1^H$ and an angle of 90° with $\mathbf{p}_{34}$, as evident from Fig. 15(a). The corresponding q^H and q^S are related to the integer ratio m/n by

$$q^S = q^H\sqrt{[(1+m/n)^2 + (m/n)^2]}, \tag{24}$$

using Eq. (21).

The physics of incommensurate structures has been developed in the context of solid state studies where the spatial extension of the systems is typically very large in comparison to the basic atomic lattice constant. In these systems quasiperiodic structures originate from additional mechanisms (i.e, in charge density waves) associated with a characteristic length scale not commensurate with the lattice constant.

In hydrodynamic pattern forming systems it is difficult to distinguish truly incommensurate patterns. Directly above the bicritical threshold the ratio q^S/q^H is virtually fixed by critical values to q_c^S/q_c^H. By tuning the experimental parameters ω and δFr, the ratio q_c^S/q_c^H can, in principle, be changed continuously in such a way that the ideal commensurability according to Eq. (24), i.e., a perfect SQL, is achieved. However, for $R > R_c$ bands of linearly unstable harmonic and subharmonic modes become accessible, permitting the system at fixed ω and δFr increasing freedom to

internally adjust the harmonic and subharmonic wave vectors to avoid incommensurability. Thus for the regular SQL any ratio q^S/q^H can be represented to arbitrary accuracy by Eq. (24) with properly chosen integers $m \equiv \bar{m}$ and $n \equiv \bar{n}$.

Unlike solid systems, finite size effects are expected to play a major role in fluid pattern formation. For values of $\bar{n}$ such that the length of the basis vectors $\bar{n}a^{SQ}$ becomes comparable to the radius of the convection cell the SQL periodicity cannot be exactly realized in the physical system. The same problem arises in our numerical simulations with a limited resolution on a finite square. It appears difficult to predict from basic principles how our system will respond to this inherent frustration. The unit cell is required to be considerably smaller than the calculational domain. In fact, SQLs observed in numerical simulations demonstrate a pronounced tendency to select a wave-number ratio q^S/q^H that satisfies Eq. (24) through a rational m/n with *small* $n = 1, 2, 3$ to an accuracy of better than 1%. On the other hand, the exact representation, to within our numerical precision, of q^S/q^H in Eq. (24) requires a rational $\bar{m}/\bar{n}$, where $\bar{m}/\bar{n} \neq m/n$, potentially with a large $\bar{n}$. The decomposition

$$\mathbf{p}_{12} = \frac{m}{n}(\mathbf{q}_1^H + \mathbf{q}_2^H) + \left(\frac{\bar{m}}{\bar{n}} - \frac{m}{n}\right)(\mathbf{q}_1^H + \mathbf{q}_2^H) \qquad (25)$$

and an analogous one for $\mathbf{p}_{34}$ indicate that the actual SQC pattern should be interpreted as a SQL constructed with a small n (i.e., locally with a small periodicity cell), that is modulated on a large scale $2\pi/[|(\bar{m}/\bar{n}) - (m/n)|q^H]$. The corresponding notion of *modulated SQL* is probably the appropriate characterization of physical superlattices in a finite domain, when some freedom is left to the system in selecting the resonating wave vectors from a band, as in our case. This definition is also appropriate for the experimental picture in Fig. 4(a), where the deviation from the rectangular tetrad can be interpreted in analogy to Eq. (25) as a modulated superlattice.

To augment our experimental findings the numerical analysis focuses on the robustness of complex-ordered patterns. Typically our simulations use random initial conditions on a nonadapted calculational grid. To some extent the system has the freedom to choose optimal angles α to orient the square backbone according to Eq. (19) as well as q^H and q^S. As a first example, the SQL shown in Fig. 4(b) corresponds to $m/n = 3/2$, which yields $q^S/q^H = 2.915$ according to Eq. (24). This value is practically identical to the ratio $q^S/q^H = 2.912$ that the system selects in simulations using random initial conditions. The two basis vectors $2\mathbf{a}_1^H$ and $2\mathbf{a}_2^H$ [Eqs. (20)], include angles of $\approx 25°$ and $\approx 115°$ with the x axis, respectively. Inspection of Fig. 4(b) confirms that the lattice constant is 2 times the lattice constant of the square backbone ($n = 2$). In the vicinity of bicritical points at other values of ω numerical superlattices realized different n values. The pattern shown in Fig. 17(a) has $q^S/q^H = 2.236$. According to Eq. (24) this corresponds to $m/n = 1$. With $n = 1$ the lattice is indeed spanned by the harmonic basis vectors $\mathbf{a}_i^H$ constructed according to Eqs. (19) and (20) with $\alpha = 12.5°$.

Figure 17(b) is a more complex SQL that is observed when using random initial conditions. The square backbone is spanned in Fourier space by the vectors

$$\mathbf{q}_1^H = q^H(1,0) \quad \text{and} \quad \mathbf{q}_2^H = q^H(0,1). \qquad (26)$$

The most symmetric realization of a SQL, consistent with the duplicate tetrad condition in Eqs. (15) and (16) and in agreement with Fig. 17(d), is achieved by the following definitions of the wave vectors $\mathbf{q}_i^S$ ($i = 1, \ldots, 6$):

$$\mathbf{q}_2^S = \frac{m}{n}(\mathbf{q}_1^H + \mathbf{q}_2^H), \quad \mathbf{q}_{1,3}^S = \mathbf{q}_2^S \pm (\mathbf{q}_1^H - \mathbf{q}_2^H), \qquad (27)$$

$$\mathbf{q}_5^S = \frac{m}{n}(\mathbf{q}_2^H - \mathbf{q}_1^H), \quad \mathbf{q}_{4,6}^S = \mathbf{q}_5^S \pm (\mathbf{q}_1^H + \mathbf{q}_2^H), \qquad (28)$$

where m/n is a rational number. The magnitudes of the various wave numbers in Eqs. (27) and (28) satisfy

$$q_i^S = \begin{cases} q^H \sqrt{2\left[1 + \left(\dfrac{m}{n}\right)^2\right]}, & i = 1,3,4,6, \\[4mm] q^H \sqrt{2\left(\dfrac{m}{n}\right)^2}, & i = 2,5. \end{cases} \qquad (29)$$

In fact the simulation shown in Fig. 17(b) has practically locked into this ideal double tetrad SQL with $m = 7$ and $n = 2$. The deviation from the corresponding ratios $q_1^S/q^H = 5.147$ and $q_2^S/q^H = 4.95$ according to Eq. (24) are less than 1%. It requires concentration on the small white dots between the stars in Fig. 17(b) to identify the primitive unit cell that has $n = 2$, four times larger than the square backbone one.

In Figs. 18(a) and 18(b) a rhombic background pattern is observed; it is spanned by the wave vectors

$$\mathbf{q}_{1,2}^H = q^H(\cos(\alpha), \pm \sin(\alpha)), \quad \alpha \approx 30°. \qquad (30)$$

The corresponding basis vectors in real space are given by

$$\mathbf{a}_{1,2}^H = \frac{2\pi}{q^H}(\pm \cos(90 - \alpha), \sin(90 - \alpha)). \qquad (31)$$

If the subharmonic wave vectors $\mathbf{q}_1^S$ and $\mathbf{q}_2^S$ are constructed in line with Eqs. (22), the pattern is a *rhombic superlattice* (RSL). In analogy to Eq. (24) the following relation holds:

$$q^S = q^H \sqrt{\left[\left(1 + \frac{m}{n}\right)^2 + \left(\frac{m}{n}\right)^2 + \frac{m}{n}\left(\frac{m}{n} + 1\right)\cos(\alpha)\right]}. \qquad (32)$$

For $q^S/q^H = 2.08$ we find $m/n = 0.687 \approx 2/3$. In fact, on inspection of Fig. (18) periodicity with three ($n = 3$) rhombic lattice constants along $\mathbf{a}_i$ ($i = 1, 2$) which enclose angles 60° and 120° with the x axis, respectively can be observed.

Finally we address the stripe superlattice shown in Fig. 6(a). In the spectral domain all of the stimulated peaks [Fig. 6(b)] may be spanned by two wave vectors $\mathbf{q}_i$ ($i = 1, 2$). Correspondingly, there always exists position space basis vectors $\mathbf{a}_i$ ($i = 1, 2$) which fulfill the conditions $\mathbf{q}_i \cdot \mathbf{a}_j = 2\pi\delta_{i,j}$ ($i, j = 1, 2$). Such complex-ordered patterns are then always periodic and thereby superlattices.

In this section we have described (modulated) superlattices on a geometrical basis. Whether they are physically realized depends on the wave-number ratio q^H/q^S which is roughly determined by the critical values at a bicritical point q_{2c}^H, q_{2c}^S. The wave-number ratio can be modified via the modulation amplitude and frequency. In addition the system will exploit the wave-number dependence of the cross coefficients (see Sec. IV), to optimize the tetrad resonance. This might explain the observations of $q^H/q^S \neq q_{2c}^H/q_{2c}^S$ made in experiments and simulations. Such features are certainly not easy to capture by simple models of coupled amplitude equations. Finally, the superlattice point group has not been discussed here, which would require additional considerations of the phases of the amplitudes.

VII. CONCLUSIONS

In summary, we have reported an investigation of spatially complex patterns composed of multiple scales that are found in fluid motion driven by both a vertical thermal gradient and time periodic vertical acceleration. To the best of our knowledge, these patterns are novel and the first examples of complex order reported in a convection experiment. All of these patterns are observed in a coexistence parameter region and are thus composed of two distinct wave numbers with modes at one q responding harmonically to the oscillation frequency and modes at the other q responding subharmonically to ω. The complex order is shown to be governed by certain resonant tetrad conditions.

With the exception of the immediate vicinity above the bicritical point, experiments and simulations of the Boussinesq equations were found to be in excellent agreement. While in simulations SQC solutions seem to bifurcate directly at the bicritical point from the ground state, this is not observed in the experiments. We find this disagreement is due to the broken midplane reflection symmetry of the fluid layer caused by relatively strong temperature variations of the material parameters. This allows for an additional three-mode resonance harmful in competition with the resonant tetrads. In fact some simulations that accounted for weakly broken inversion symmetry confirmed the experimental features.

Fairly complicated patterns with intermittent dynamics between harmonic and subharmonic patches have been identified in the experiments when changing systematically the parameters, either from pure harmonic or pure subharmonic states. The transition to such a coexistence as well as the locking into extended SQCs could in general be identified in the power spectra.

For the classification of the various types of quasiperiodic patterns in this paper, which exist also when heating from above, certain conditions for the arrangement of the harmonic and subharmonic wave vectors have been presented to study the possibility of periodic superlattice patterns. Considering the role of finite size effects we propose to understand the quasiperiodic crystals in our experiment in terms of modulated superlattices.

It is worth noting that modulation of convective flow can be achieved by other ways than imposing time-dependent acceleration; for example, several investigations have examined the related problem of modulated convection due to time-periodic oscillation of ΔT about nonzero mean [36–43]. In principle, such studies can also investigate interesting dynamics arising near harmonic and subharmonic bicritical points. However, experimental realizations have been restricted to slow temporal modulations due to time delays between the drive and the system response. These prevent imposing spatially uniform modulation at frequencies that are sufficiently large to observe subharmonic convection or to probe the competition between harmonic and subharmonic modes.

Complex-ordered patterns have been observed in other systems capable of forming macroscopic patterns. Previously reported examples can be separated into two broad classes, fluidlike and optical. With the exception of a ferrofluid case [15] all of the previous fluidlike systems have been variations of the Faraday apparatus [44]. In these systems waves on the free surface of a vertically vibrated fluid layer display quasiperiodic crystals [10,11] and superlattices [12,14]. The main difference between these systems and the present one is that a resonant interaction of waves must satisfy relations between both wave vectors $\mathbf{k}_i$ and frequencies $\omega(\mathbf{k}_i)$, defined by dispersion relations. In the majority of Faraday examples the experiment is designed to break the subharmonic temporal symmetry to allow three-wave interactions. Edwards and Fauve [10] first excluded this symmetry by including two driving frequencies to produce a harmonic response; a method used by a majority of subsequent investigators [11–14]. Harmonic response has also been achieved when using a single drive ω by tuning ω to match the intrinsic time scale of a viscoelastic fluid [45]. In the absence of inversion symmetry *resonant triads* are allowed and are found to be the selection mechanism for complex-ordered patterns.

Qualitatively similar, complex-ordered patterns have been observed in optical studies [16] involving a nonlinear medium. Pattern symmetries in these studies are either externally imposed by rotation of the optical field in a nonlinear cavity [16] or as a more natural result of the configuration [8,17]. In most cases resonant triads found to produce complex order are intentionally constructed. For completeness, we also mention that quasipatterns are a possibility in reaction-diffusion systems as a result of resonant triads [46,47].

Complex-ordered patterns produced by resonant tetrads have previously been reported in the Faraday system. While resonant triads are typically studied in these systems, the first reported macroscopic quasiperiodic crystals were by Christiansen, Alstrøm, and Levinsen [48] using a Newtonian fluid and a single forcing frequency. In this case the authors found quasiperiodic crystals resulting from four-wave resonant interactions near onset, consistent with the temporal symmetry making the cubic amplitude equation term the lowest order nonlinearity present. Recently, complex order resulting from four-wave interactions in a Faraday experiment were again reported [14]; in this case when using 2 frequency forcing. However, recent studies have focused on resonant triads and reporting complex-order due to resonant tetrads as an exception.

Four-wave interactions can be more significant to the dynamics of physical systems than three-wave interactions in

other systems. Considering the problem of ocean wave generation Phillips [49,50] studied inviscid gravity waves in deep water. In this case the wave is characterized by a two-dimensional wave vector **k** and its frequency ω determined by the nonlinear dispersion relation $\omega = \omega(k)$. The reported results indicate that at least *four* modes are required for a resonant coupling

$$\mathbf{k_1} + \mathbf{k_2} = \mathbf{k_3} + \mathbf{k_4},$$

$$\omega_1 + \omega_2 = \omega_3 + \omega_4, \quad \omega_i = \omega(k_i). \tag{33}$$

Consequently four-wave resonances play the dominant role in energy transfer between wave components, while the effects of three-wave interactions remain negligible. In this case the resonant coupling of the mode amplitudes leads to four coupled amplitude equations that are analogous to our case in conceptual structure.

In this paper we have not systematically investigated the stability of superlattices and their bifurcations. Our evidence indicates the resonant tetrads shown in Figs. 15 and 4 have bifurcated directly from the trivial state. There is some analogy to the case of superlattice-one (SL_I) patterns in the Faraday case [11,51]. In contrast the superlattice-two (Sl_II) patterns in Ref. [11] arise from a secondary spatial period-multiplying bifurcation from hexagons [52]. This case bears some analogy to the transition from stripe superlattices (Fig. 6) to square quasiperiodic crystals and square superlattices. An interesting outstanding question is the choice of the system to switch from simple superlattices [as in Fig. 6(a) with $n=1$] with the periodicity of the underlying square lattice to the case of a basis cell of double extension [see $n=2$, Fig. 4(b)] with varying ratio of q^S/q^H. It would also be interesting to determine whether other superlattices described as transients in simple Rayleigh-Bénard convection in the nonlinear regime [53,54] could be realized as stationary patterns.

[1] M. Cross and P. Hohenberg, Rev. Mod. Phys. **65**, 851 (1993).

[2] E. Bodenschatz, W. Pesch, and G. Ahlers, Annu. Rev. Fluid Mech. **32**, 709 (2000).

[3] F. Busse, J. Fluid Mech. **30**, 625 (1967).

[4] J. P. Gollub and M. C. Cross, Nature (London) **404**, 710 (2000).

[5] F. Busse and R. Clever, *Mathematical Modelling and Simulation in Hydrodynamic Stability* (World Scientific, Singapore, 1996), pp. 15–34.

[6] F. Busse and R. Clever, Phys. Rev. Lett. **81**, 341 (1998).

[7] K. E. Daniels and E. Bodenschatz, Phys. Rev. Lett. **88**, 034501 (2002).

[8] L. M. Pismen and B. Y. Rubenstein, Chaos, Solitons Fractals **10**, 761 (1999).

[9] R. Lifshitz, Rev. Mod. Phys. **69**, 1181 (1997).

[10] W. Edwards and S. Fauve, Phys. Rev. E **47**, R788 (1993).

[11] A. Kudrolli, B. Pier, and J. Gollub, Physica D **123**, 99 (1998).

[12] H. Arbell and J. Fineberg, Phys. Rev. Lett. **81**, 4384 (1998).

[13] H. Arbell and J. Fineberg, Phys. Rev. Lett. **84**, 654 (2000).

[14] H. Arbell and J. Fineberg, Phys. Rev. E **65**, 036224 (2002).

[15] H. J. Pi, S. Y. Park, J. Lee, and K. J. Lee, Phys. Rev. Lett. **84**, 5316 (2000).

[16] E. Pampaloni, S. Residori, S. Soria, and F. Arecchi, Phys. Rev. Lett. **78**, 1042 (1997).

[17] R. Herrero, E. G. Westhoff, A. Aumann, T. Ackemann, Y. A. Logvin, and W. Lange, Phys. Rev. Lett. **82**, 4627 (1999).

[18] C. M. Topaz and M. Silber, Physica D **172**, 1 (2002).

[19] P. M. Gresho and R. L. Sani, J. Fluid Mech. **40**, 783 (1970).

[20] R. Clever, G. Schubert, and F. Busse, J. Fluid Mech. **253**, 663 (1993).

[21] R. Clever, G. Schubert, and F. Busse, Phys. Fluids A **5**, 2430 (1993).

[22] J. Rogers, M. Schatz, J. Bougie, and J. Swift, Phys. Rev. Lett. **84**, 87 (2000).

[23] J. Rogers, M. Schatz, O. Brausch, and W. Pesch, Phys. Rev. Lett. **85**, 4281 (2000).

[24] P. L. Gal and V. Croquette, Phys. Fluids **31**, 3440 (1988).

[25] M. Westerburg and F. Busse, J. Fluid Mech. **432**, 351 (2001).

[26] W. A. Tokaruk, T. Molteno, and S. W. Morris, Phys. Rev. Lett. **84**, 3590 (2000).

[27] M. Dominguez-Lerma, G. Ahlers, and D. S. Cannell, Phys. Rev. E **52**, 6159 (1995).

[28] V. Croquette, Contemp. Phys. **30**, 113 (1989).

[29] J. de Bruyn, E. Bodenschatz, S. Morris, S. Trainoff, Y. Hu, D. Cannell, and G. Ahlers, Rev. Sci. Instrum. **67**, 2043 (1996).

[30] W. Pesch, Chaos **6**, 348 (1996).

[31] S. Biringen and L. J. Peltier, Phys. Fluids A **2**, 754 (1990).

[32] U. E. Volmar and H. W. Müller, Phys. Rev. E **56**, 5423 (1997).

[33] M. Cross, Phys. Rev. A **25**, 1065 (1982).

[34] A. Rucklidge and W. Rucklidge, Physica D **178**, 62 (2003).

[35] M. Higuera, H. Riecke, and M. Silber, SIAM J. Appl. Dyn. Syst. **3**, 463 (2004).

[36] G. M. Homsy, J. Fluid Mech. **62**, 387 (1974).

[37] R. G. Finucane and R. E. Kelly, Int. J. Heat Mass Transfer **19**, 71 (1976).

[38] M. N. Roppo, S. H. Davis, and S. Rosenblat, Phys. Fluids **27**, 796 (1984).

[39] G. Ahlers, P. Hohenberg, and M. Lücke, Phys. Rev. A **32**, 3493 (1985).

[40] G. Ahlers, P. Hohenberg, and M. Lücke, Phys. Rev. A **32**, 3519 (1985).

[41] P. Hohenberg and J. Swift, Phys. Rev. A **35**, 3855 (1987).

[42] J. J. Niemela and R. J. Donnelly, Phys. Rev. Lett. **59**, 2431 (1987).

[43] C. W. Meyer, D. S. Cannell, and G. Ahlers, Phys. Rev. A **45**, 8583 (1992).

[44] H. Müller, R. Friedrich, and D. Papathanassiou, *Lecture Notes in Physics* (Springer, Berlin, 1998), pp. 230–265.

[45] C. Wagner, H. Müller, and K. Knorr, Phys. Rev. Lett. **83**, 308 (1999).

[46] M. Bachir, S. Métens, P. Borckmans, and G. Dewel, Europhys. Lett. **54**, 612 (2001).

[47] G. Dewel, M. Bachir, P. Borckmans, and S. Métens, C. R. Acad. Sci., Ser. IIb: Mec., Phys., Chim., Astron. **329**, 411 (2001).

[48] B. Christiansen, P. Alstrøm, and M. T. Levinsen, Phys. Rev. Lett. **68**, 2157 (1992).

[49] O. Phillips, J. Fluid Mech. **9**, 193 (1960).

[50] O. Phillips, J. Fluid Mech. **11**, 143 (1961).

[51] M. Silber and M. R. Proctor, Phys. Rev. Lett. **81**, 2450 (1998).

[52] D. Tse, A. Rucklidge, R. Hoyle, and M. Silber, Physica D **146**, 367 (2000).

[53] D. White, J. Fluid Mech. **191**, 247 (1988).

[54] D. McKenzie, J. Fluid Mech. **191**, 287 (1988).